X-ray Point Sources in The Central Region of M31 as seen by *Chandra*

Albert K.H. Kong, Michael R. Garcia, Francis A. Primini, Stephen S. Murray, Rosanne Di Stefano[1] and Jeffrey E. McClintock

Harvard-Smithsonian Center for Astrophysics, 60 Garden Street, Cambridge, MA 02138

ABSTRACT

We report on *Chandra* observations of the central region of M31. By combining eight *Chandra* ACIS-I observations taken between 1999 and 2001, we have identified 204 X-ray sources within the central $\sim 17' \times 17'$ region of M31, with a detection limit of $\sim 2 \times 10^{35}\,\mathrm{erg\,s^{-1}}$. Of these 204 sources, 21 are identified with globular clusters, 2 with supernova remnants, 8 with planetary nebula, and 11 with supersoft sources. By comparing individual images, about 50% of the sources are variable on time scales of months. We also found 14 transients, with light curves resembling those seen in our Galaxy. We also extracted the energy spectra of the 20 brightest sources; they can be well fit by a single power-law with a mean photon index of 1.8. The spectral shapes of 12 sources are shown to be variable, suggesting that they went through state changes. The luminosity function of all the point sources is consistent with previous observations (a broken power-law with a luminosity break at $1.7 \times 10^{37}\,\mathrm{erg\,s^{-1}}$). However, when the X-ray sources in different regions are considered separately, different luminosity functions are obtained. This indicates that the star-formation history might be different in different regions.

Subject headings: galaxies: individual (M31) — X-rays: galaxies — X-rays: stars

1. Introduction

At a distance of $\sim$ 800 kpc, M31 provides us with a prime opportunity to study the global properties of a galaxy which is similar to our Milky Way. As M31 and the Milky Way share similar morphology and size, comparisons between their X-ray properties can be enlightening. Even though M31 is further away, studies of X-ray sources within it are simplified relative to the Galaxy for several reasons. Firstly, the distance is well known, allowing us to determine X-ray luminosities accurately. Secondly, the extinction of X-ray sources within M31 is much lower than that typical of sources in the Galaxy, which enables us to study the X-ray properties of M31 over a wider energy band. Finally, the nearly face-on orientation of M31 allows us to more easily determine the location of X-ray sources within (or outside of) spiral arms, the galactic bulge, or halo.

[1]also Department of Physics and Astronomy, Tufts University, Medford, MA 02155

M31 has been observed extensively by several earlier X-ray missions. The first detailed observations were made with the *Einstein* IPC and HRI (Trinchieri & Fabbiano 1991) and over 100 sources were detected at a detection limit of $\sim 10^{36}$ erg s^{-1} (0.2–4.0 keV). Subsequent *ROSAT* HRI observations of the central $\sim 34'$ revealed 86 sources at a similar detection limit (Primini, Forman, & Jones 1993, hereafter PFJ93). A comparison of the *Einstein* and *ROSAT* source lists showed that ∼42% of the sources within the central $7.5'$ region were variable. Recently, two deep and extensive *ROSAT* PSPC surveys have identified 560 point sources in the entire disk of M31 (Supper et al. 1997, 2001; hereafter Su97, Su01). The detection limit of this survey was $\sim 5 \times 10^{35}$ erg s^{-1} (0.1–2 keV). These 560 sources include 33 globular clusters, 16 supernova remnants, 15 supersoft sources, 55 foreground stars and 10 background objects.

M31 was observed by *Chandra* and *XMM-Newton* soon after these observatories were launched. In the first observation (8.8 ks) of the core region by *Chandra* in 1999 October, 121 point sources were identified within the central $17' \times 17'$ region and the nucleus, which had been seen as one source by previous missions, was nicely resolved into five point sources (Garcia et al. 2000a). Moreover, a bright transient was discovered $\sim 26''$ from the nucleus. A relatively deeper *XMM-Newton* observation (34.8 ks) was made in 2000 June; 116 sources were detected down to a limiting luminosity of 6×10^{35} erg s^{-1} (0.3–12 kpc; Shirey et al. 2001) and a pulsating supersoft transient with a periodicity of $\sim$ 865 s was discovered (Osborne et al. 2001). Moreover, both *Chandra* (Garcia et al. 2001a; Primini et al. 2000) and *XMM-Newton* (Shirey et al. 2001) observations confirmed that the unresolved X-ray emission in the core region is much softer than most of the resolved X-ray sources in that region. Fifteen X-ray point sources are newly associated with globular clusters (Di Stefano et al. 2002), which when combined with the previous *ROSAT* results (Su01) brings the total number of M31 globular clusters with detected X-ray emission to 48. The X-ray luminosity of these globular clusters appears to be substantially higher than clusters in the Galaxy; for example, in M31 $\sim 1/3$ of the clusters have luminosities $L_X > 10^{37}$ erg s^{-1} (0.5–7.0 keV). *Chandra* and *XMM-Newton* also discovered several bright ($L_X > 10^{37}$ erg s^{-1}) transients in M31 and M32 (Garcia et al. 2000a; Garcia et al. 2000b; Osborne et al. 2001; Shirey 2001; Kong et al. 2001; Garcia et al. 2001b). The brightest of these reached a peak luminosity of $L_X \sim 3 \times 10^{38}$ erg s^{-1}.

We report herein the properties of the point sources in the central $\sim 17' \times 17'$ region of M31 as deduced from eight separate $\sim$ 5ks ACIS-I observations spanning $\sim$ 1.5 years. The detection limit (while variable) is $\sim 2 \times 10^{35}$erg s^{-1} (0.3–7 keV) across most of this region. In addition to a source catalog, we discuss the overall spectral properties, temporal variability and luminosity function of these sources. The brighter sources have sufficient counts to allow meaningful searches for spectral variability, allowing comparison to Galactic sources. The main focus of this paper is on the complete source list and the overall properties of point sources in M31. In a series of companion papers, we will discuss the diffuse emission (for instance, see Primini et al. 2000 and Dosaj et al. 2001 for a preliminary analysis), the X-ray emission from the central supermassive black hole (Garcia et al. 2002), temporal and spectral variability (Kong et al., in preparation) and

supersoft source populations (Di Stefano et al., in preparation)

In this paper, we adopt a distance of 780 kpc (Stanek & Garnavich 1998; Macri et al. 2001) and assume a hydrogen column density equal to the Galactic value of $\sim 7 \times 10^{20}$ cm^{-2} (Dickey & Lockman 1990) unless otherwise specified. The quoted errors throughout this paper are at 90% confidence, unless otherwise specified.

2. Observations and Data Reduction

M31 was observed with *Chandra* regularly as part of the AO-1 and AO-2 GTO program during 1999–2001. The program was designed to search for transients. The observations consist of a series of HRC snapshots ($\sim$ 1 ks) that cover the entire galaxy. If a transient is discovered in the HRC mosaic, then a follow-up ACIS image ($\sim$ 5 ks) of the transient is obtained; otherwise an ACIS image of the nucleus is obtained. In this paper we focus only on the ACIS-I (I0, I1, I2 and I3) data obtained for the central $16.9' \times 16.9'$ region of M31. These data consist of 8 separate observations, with exposure times ranging from 4 to 8.8 ks. The details of the observations are given in Table 1. The nuclear region of M31 was placed near the aim-point of the ACIS-I array. The focal-plane temperature was -110°C during the first four observations, and -120°C for the others. The observations were made at various spacecraft roll angles; consequently, the total region covered by the observations is slightly larger than $16.9' \times 16.9'$, and sources near the outer edge of ACIS are not observable in all eight exposures.

All data were telemetered in Faint mode and were collected with a frame transfer time of 3.2 s. In order to reduce the instrumental background, only data with *ASCA* grades of 0, 2, 3, 4, and 6 were included. We selected data free from bad columns, hot pixels and columns close to the borders of each ACIS chip node. The standard $0.5''$ pixel randomization was also removed. Only events with photon energies in the range of 0.3–7.0 keV were included in our analysis. We inspected the background count rates from the ACIS-S3 chip for all of the observations; except for the first observation, no significant background flares were found. For the first observation, periods with high background were rejected, resulting in an effective exposure time of 8.8 ks out of 17.5 ks (see Garcia et al. 2000a for details of this observation).

The data reduction and analysis was done with CIAO v2.1 [2]. Some of the image analysis was done with IRAF, while the spectra were analyzed with XSPEC v11 [3].

[2]http://asc.harvard.edu/ciao/

[3]http://heasarc.gsfc.nasa.gov/docs/xanadu/xspec/index.html

3. Analysis

3.1. X-ray Images

In order to create a deep image suitable for the detection of faint sources, the eight observations were combined into a single stacked image. The rms uncertainty of the aspect solution of *Chandra* is $\sim 1''$, but there can be systematic errors (up to $2''$) for specific ACIS-I observations [4]. These errors are larger than the PSF, and therefore could degrade the PSF of the stacked image. We removed these errors by registering all the data sets to the coordinate frame of OBSID00312 using 12 bright X-ray sources within $\sim 5'$ of the aim-point. The positions of these sources were determined from the weighted centroid of the counts in a $0.5''$ pixel (= one ACIS pixel) image. The cross registration of the eight data sets is accurate to $\sim 0.4''$.

Because the nuclear region of M31 is particularly crowded (see Garcia et al. 2000a), we were concerned that the $\sim 0.4''$ accuracy achieved above would be insufficient. We therefore repeated the procedure above on an image of the central $2' \times 2'$, but used a pixel size of $1/8''$ (= 1/4 ACIS pixel) scale. This improved the registration in the nuclear region to $0.25''$.

The *absolute* astrometry of these images is still limited by the *Chandra* aspect solution to $\sim 1''$. In order to allow comparison to *HST* images (which also have absolute astrometric errors of $\sim 1''$), we registered the combined *Chandra* images to a merged *HST* image using two globular clusters detected in both data sets (see Garcia et al. 2002 for details). The exposure of the combined images ranges between 4 ks (at the extreme edges) and 39.7 ks (in the center). More than 170 sources have a total integration time of 30 ks.

Figure 1 shows the stacked "true color" image of M31, which is a composite of images from soft (0.3–1.0 keV), middle (1–2 keV) and hard (2–7 keV) bands. Soft sources appear red, moderately hard sources appear green, and the hardest sources appear blue. The image has been corrected for exposure and smoothed slightly with a Gaussian ($\sigma = 0.5''$) in order to improve the appearance of point sources. In Figure 2, we show the "true color" image of the central $2' \times 2'$ region of M31 in $1/8''$ pixel resolution, with the possible nuclear counterpart (M31*) marked (Garcia et al. 2002).

3.2. Source Detection

Discrete sources in the stacked image were found with WAVDETECT (Freeman et al. 2002), a wavelet detection algorithm implemented within CIAO. The central $2' \times 2'$ region was treated separately by using the $1/8''$ pixel image. The two source lists were combined into the master source list shown in Table 2. We set the detection threshold to be 10^{-6} and carried out the wavelet analysis at 9 scales (1, $\sqrt{2}$, 2, $2\sqrt{2}$, 4, $4\sqrt{2}$, 8, $8\sqrt{2}$ and 16). This detection threshold corresponds

[4] see http://asc.harvard.edu/mta/ASPECT/

to < 1 false detection due to statistical fluctuations in the background. We then repeated this procedure on the annular square region between $2'$ and $8'$ in size using an image with $1/2''$ pixels. On the region outside of the $8' \times 8'$ square we used an image with $2''$ pixels. A total of 205 sources were detected. Source count rates were determined via aperture photometry. The radius of the aperture was varied with average off axis angle in order to match the 90% encircled energy function. The average off axis angle was computed for each source based on the off axis angles of the eight observations weighted by their exposure times. The extraction radius varies from $\sim 1''$ near the aim-point to $\sim 17''$ for the sources with the largest off axis angles.

Background was extracted from an annulus centered on each source. In some cases, for example in the nuclear region, we modified the extraction region to avoid nearby sources. It was also necessary to modify the extraction radius for some faint sources that are close to more luminous sources. Every extraction region was examined carefully in the image. The count rate was corrected for exposure, background variation and instrumental PSF. We examined the image of each detected source, and found only one case in which the detection was clearly spurious (this source had signal-to-noise ratio S/N < 2).

Table 2 lists the 204 sources in our catalog, sorted in order of increasing R.A. The columns give the source number, the IAU approved name, the position (J2000), the net counts, the count rate and 1-σ error, hardness ratios (see §3.4) and the 0.3–7.0 keV luminosity. The source numbers have a prefix of r1, r2 and r3. The r1 sources are located in the central $2' \times 2'$ or "inner bulge" region. The r2 sources are located within the central $8' \times 8'$ excluding the inner bulge region; we refer to this annular region as the "outer bulge". The r3 sources are located outside the central $8' \times 8'$ in the "disk" region. This nomenclature is based on optical studies (Morton, Andereck & Bernard 1977); a similar classification was also used by Trinchieri & Fabbiano (1991). The conversion to luminosities assumes an absorbed power-law spectrum with a photon index of 1.7 and $N_H = 10^{21}$ cm^{-2}, which is the typical spectrum of a point source in M31 (Shirey et al. 2001). All sources in the catalog have S/N > 2.5 and only 5 have S/N < 3. The detection limit for the sources varies across the image due to the variations of exposure time, background and instrumental PSF, and is highest near the edges where the PSF broadens rapidly and exposure time is lowest. Over the inner $4'$ of the field, the detection limit is 2.1×10^{-4} counts s^{-1}, which is equivalent to $L_X \sim 2 \times 10^{35}$ erg s^{-1}.

3.3. Source Identification

Tables 3–5 summarize the results of matching our new ACIS source catalog with existing catalogs of M31 objects. Table 3 lists the number of matches found in each of the catalogs we searched, and also the number of accidental (spurious) matches expected. Table 4 lists the catalog identifications of the ACIS sources and the offset between the cataloged object and the ACIS source. Table 5 itemizes the matches between our ACIS catalog and the *ROSAT* HRI source list (PFJ93). We varied the search radius based on the accuracy of the various catalogs (increasing it as needed),

and also based on the density of sources in the catalogs (reducing it in order to limit accidental matches).

We used the following catalogs and corresponding search radii:

ROSAT sources: the *ROSAT* HRI catalog (PFJ93) — 6″ search radius.

Globular clusters: the Bologna catalog (Battistini et al. 1987), the catalog by Magnier (1993), and a recent catalog based on *HST* data by Barmby (2001) — 3″ search radius for all three.

Supernova remnants: the lists by d'Odorico et al. (1980), Braun & Walterbos (1993), and Magnier et al. (1995) — 10″ search radius.

Planetary nebulae: the catalogs by Ford & Jacoby (1978) and Ciardullo et al. (1989)— 3″ search radius.

Extragalactic objects: the NASA/IPAC Extragalactic Database (NED) and SIMBAD — 3″ search radius.

M31 stars: the catalog of 485,425 objects (mainly stars) by Haiman et al. (1994) and the SIMBAD — 1″ search radius.

Stellar Nova: as reported in the IAUC during the period covered by our observations — 3″ search radius.

OB Associations: the catalog of 174 OB associations within M31 identified by Magnier et al. 1993) — 3″ search radius.

In order to estimate the accidental correlation rate, we used a technique similar to that described by Hornschemeier et al. (2001). We shifted all the *Chandra* sources by 10″ to the northeast, northwest, southeast, and southwest, and ran the search for each of the catalogs. The results were averaged to estimate the accidental matching rate listed in Table 3. With the exception of the large catalog of M31 stars, the accidental matching rates are generally small, therefore justifying our choice of search radius. For example, the average accidental matching rate with *ROSAT* sources is 7.5, which is $< 10\%$ of the total number of *ROSAT* matches found (77).

We find two matches with SNR, but predict a random match rate (1.5) that is similar to what we find. However, the unusual nature of the two sources which match with the SNR catalog leads us to believe that these matches are real. Both of these *Chandra* sources have relatively low hardness ratio values (see §3.4) and *Chandra* source r3-63 is resolved into a ring-like object (Kong et al. 2002). Both of these identifications are listed in Table 4, and the total number of true SNR IDs is listed in Table 3 as two.

We found 40 *Chandra* sources within 1″ of objects in the Haiman et al. (1994) catalog, which consists mainly of stars in the field of M31. The number of accidental matches even with this small 1″ search radius is 34.75, nearly equal to the number found! This is due to the very high density of objects in this catalog, and leads us to expect that most of the 40 matches are spurious.

However, one can test these possible identifications with the spectral (or hardness ratio) data. X-ray emission from stars is relatively soft; for instance, the PSPC survey (Su97) showed that the energy spectrum of a foreground star can be best fitted by a Raymond-Smith model with $kT_{RS} \sim 1$ keV or a power-law model with a photon index $\alpha \gtrsim 3$. However the *Chandra* sources which have a sufficient number of counts for spectral analysis (see §3.5) have much harder spectra ($\alpha \sim 1 - 2$) and are therefore unlikely to be stars. In the remaining cases where there are too few counts we examined the hardness ratio (HR2; see §3.5). If the ratio is inconsistent with a soft spectrum (i.e., if HR2 is greater than -0.5), we similarly rule out a stellar association. In this way we rule out 35 of the possible 40 matches. Table 4 lists the remaining 5 possible stellar identifications. We note the (fortuitous?) agreement in numbers between the number of sources with soft spectra (5) and the accidental matching rate which leads us to expect that ~ 5 out of our possible 40 matches may be real. These numbers are summarized in Table 3.

We find that 77 *Chandra* sources have counterparts in the *ROSAT* HRI catalog (see Table 5). The remaining 127 ($= 204 - 77$) *Chandra* sources were not detected in the *ROSAT* HRI catalog, presumably because they are below the *ROSAT* detection limit or are variable. The *Chandra* catalog extends $\sim 5\times$ fainter than the *ROSAT* HRI catalog. We have not compared our *Chandra* catalog to the new complete *ROSAT* PSPC catalog (Su01) because the later catalog covers a much larger area and has substantially lower resolution, making it less appropriate to compare to this ACIS data than the HRI catalog. We note that in 5 cases the *ROSAT* HRI sources match up with 2 or more *Chandra* sources, indicating either that these *ROSAT* sources have been resolved by *Chandra* or that one (or more) of the *Chandra* sources is transient. Alternatively, we note that we expect ~ 7.5 spurious matches with *ROSAT* sources, so something like $\sim 10\%$ of these multiple matches may be spurious. The expected numbers of spurious matches leads us to list the "true" number of matches as 69 in Table 3.

We identify 22 *Chandra* sources with globular clusters (see Table 4). Twelve of these globular clusters are identified as X-ray sources for the first time. Because globular clusters are sometimes used to register M31 images taken at different wavelengths, it may be worth noting that the average offset between the X-ray and optical positions is $1.6''$. *Chandra* source r3-74 is within $3''$ of both mita165 and mita166, but we note that these clusters themselves are separated by only $\sim 1.5''$. We therefore allow the possibility that in reality they constitute a single cluster. This possibility, along with the number of expected spurious matches, leads us to list the number of detected globular clusters as 21 in Table 3.

We found 10 matches between *Chandra* sources and planetary nebula (PN), and expect that ~ 2.5 of these are spurious matches. Ford 316 is within $2.4''$ of both r1-21 and r1-33, both of which are in the very crowded nuclear region of M31. It seems likely that Ford 316 is associated with only one (but not both) of these *Chandra* sources. *Chandra* source r1-26 is within $3''$ of both Ford 21 and Ford 74, but it seems unlikely that both PN would be associated with a single X-ray source. While it is unclear which associations might be spurious, these multiple identifications and the expected number of spurious sources leads us to estimate that there are 8 true associations between PN and

Chandra sources (see Tables 3 and 4).

Planetary nebula in the Milky Way are in general rather weak and soft X-ray sources, with $L_X \sim 10^{30}$erg s^{-1} and kT$\sim$ 0.5 keV (Guerrero et al. 2000, 2001). The most luminous PN within our galaxy has $L_X \sim 1.3 \times 10^{32}$erg s^{-1} and kT$\sim$ 0.3 keV (Kastner, Vrtilek, & Soker 2001). These *Chandra* sources have luminosities ranging from 2×10^{35}erg s^{-1} to 5×10^{37}erg s^{-1} and (with the exception of r2-56) X-ray colors much harder than the Milky Way PN, raising the possibility that these sources are either very unusual or something other than PN. We note that the Ford & Jacoby (1978) survey identified PN on the basis of on and off band imaging within the 5007Å O [III] line. Symbiotic stars often show strong 5007Å emission and are generally soft X-ray sources of modest intensity, with the single exception of GX 1+4, which has a hard spectrum and $L_X \sim 10^{37}$erg s^{-1}. This suggests that these "PN" may in fact be GX 1+4 analogs in M31. Optical spectroscopy could help determine the nature of these sources.

We searched for matches between stellar novae as listed in the IAUC that were contemporaneous with our *Chandra* observations we found no matches within 3″. Because novae may appear as X-ray sources some time after their optical appearance, we started our search with the nova reported in IAUC 7093 (Stagni, Buonomo, & di Mille 1999 Jan), which appeared $\sim$ 10 months before our first *Chandra* observation. Other novae include those in IAUC 7218 (Modjaz and Li 1999 July), 7236 (Johnson, Modjaz, & Li 1999 Aug), 7272 (Filippenko et al. 1999 Oct), 7477 (Li, 2000 Aug), 7516 (Donato et al. 2000 Nov) and 7709 (Fiaschi, Di Mille, & Cariolato 2001 Sept). While outside of our search radius (3″), a nova found in 2001 September (IAUC 7709, Fiaschi, Di Mille & Cariolato 2001) is within 5″ of source r2-29. This *Chandra* source is positionally coincident with XMMU J004234.1+411808, which Osborne et al. (2001) suggested may be an X-ray nova. This source was not detected in the ACIS observation of 2000 June 1 (OBSID 309); it reached a peak flux in an HRC-I observation on 2000 June 6 (OBSID 273), more than one year before the optical nova (see Figure 5). We know of no cases in which the X-ray outburst of an optical nova (or an X-ray nova) proceeded the optical outburst by $\sim$ 1 year, which therefore suggests that the spatial proximity of the two events is a random coincidence. The expectation value of such events is 0.25, so this is moderately possible.

We also searched for matches with OB associations, as O and B stars may be moderate X-ray sources ($L_X < 10^{33}$erg s^{-1}, Berghofer et al. 1997). While this is well below our detection limit, a group of O and/or B stars may reach our detection threshold, and star forming regions could conceivably harbor massive X-ray binaries. However, we found no matches within our search radius of 3″.

We searched for extragalactic emission line objects as listed in NED and SIMBAD, and found a single match (r3-83, see Table 4). AGN are likely to be obscured by the bulge of M31 and therefore we expect that we may detect many AGN without optical counterparts. A better estimate to the number of such object is made based on deep field observations in the next section.

3.4. Hardness Ratios

Many of the sources in our catalog have $\lesssim 100$ counts, which makes it difficult to derive spectral parameters with meaningful constraints. However, hardness ratios can give a crude indication of the X-ray spectra in these cases. We therefore computed the hardness ratios for all the detected sources. These ratios were based on the source counts in three energy bands: S (0.3–1.0 keV), M (1–2 keV) and H (2–7 keV). The two hardness ratios are defined as HR1=(M-S)/(M+S) and HR2=(H-S)/(H+S). Table 2 lists both HR1 and HR2. Figures 3 and 4, respectively, show the color-color diagram (CD) and hardness-intensity diagram (HID) for sources with over 20 counts. We have overlaid the CD with 6 lines showing the tracks followed by representative spectra with differing values of N_H. Power-law spectra tend to occupy the top right section of the diagram, while soft blackbody models occupy the lower left. For example, a "supersoft source" (SSS) having a blackbody spectrum with a temperature of 70 eV and N_H of 10^{21} cm^{-2} would be in the lower left with HR1=−0.98 and HR2=−1. A typical AGN or X-ray binary with a power-law spectrum and a photon index $\alpha = 1.7$ would be in the extreme upper right if $N_H \geq 10^{22}$ cm^{-2}.

From the CD in Figure 3, it is clear that there are three sources with more than 20 counts and with both HR1 and HR2 consistent with −1 (r3-84, r2-12, and r3-8). This indicates that they have no counts above 1 keV, and therefore are very likely SSSs. The brightest of these three sources (r2-12) is within the central $8' \times 8'$ region and has $L_X > 10^{37}$ erg s^{-1}. This source was also detected in the *ROSAT* surveys and identified as a SSS (Su01).

We searched our catalog for other candidate SSSs, following a method analogous to that of Su97 and Kahabka (1999). These surveys identified 15 SSSs (Su97) or perhaps 16 additional SSSs (Kuhabka 1999), depending upon the selection criteria used. Candidate *Chandra* SSSs are those with HR2+$\sigma_{HR2} \leq -1$ *and* HR1 < 0, **or** HR1+$\sigma_{HR1} \leq -0.8$. There are 14 sources satisfying these conditions: r1-25, r2-12, r2-19, r2-42, r2-46, r2-56, r2-57, r3-5, r3-8, r3-63, r3-69, r3-77, r3-84, and r3-96. A single one of these (r1-25) is in the central $2' \times 2'$ region. Source r2-12 was noted as a bright SSS in both the *Einstein* and PSPC surveys. Source r3-8 was not classified as a SSS in the PSPC surveys (Su97, Su01) but was subsequently identified as a SSS based on the less tight selection criteria of Kahabka (1999). Sources r3-63 and r3-69 were both detected in the PSPC survey and were identified to be SNRs (see Table 4). Source r2-42 may be associated with an 18.6 magnitude star listed in the Ha94 catalog. Removing this star and the two SNR from consideration, we are left with 11 SSS candidates, 9 of which are newly discovered.

In the CD and HID, we have marked the three regions of M31 we have defined in different colors: the central $2' \times 2'$ (region 1) is blue, the central $8' \times 8'$ excluding the central $2' \times 2'$ (region 2) is red, and the entire field excluding the central $8' \times 8'$ (region 3) is green. All three regions show extensive overlap in both diagrams, with one clear exception: the top right hand corner of the CD is populated mainly with sources from region 3. The appearance of this figure is born out by the average hardness ratios for the three regions as listed in Table 6. Both HR1 and HR2 of region 3 are significantly ($\sim 5\sigma$) higher than the values for regions 1 and 2, which are themselves consistent

at the $\sim 2\sigma$ level. Although these sources may be intrinsically hard and within M31, many are probably strongly absorbed background AGN.

These harder sources may form a distinct group in the CD, i.e., there may be a separate clump of sources with HR1 > 0.55 and HR2 > 0.45. There are 42 sources that meet these hardness ratio criteria, 34 of them are in region 3. Based on the *Chandra* deep field observations (Brandt et al. 2001), we estimate that there should be ~ 30 serendipitous sources in our field. Thus, the majority of these will be background AGN and would therefore be strongly absorbed by the dust and gas in M31.

3.5. Temporal Variability

The eight *Chandra* ACIS-I observations described herein span nearly 2 years from 1999–2001. This is substantially longer than previous surveys by *ROSAT* (2 observations separated by ~ 1 year). In order to study long-term X-ray variability, we computed a variability parameter following PFJ93:

$$S(F_{max} - F_{min}) = \frac{|F_{max} - F_{min}|}{\sqrt{\sigma^2_{F_{max}} + \sigma^2_{F_{min}}}}, \quad (1)$$

where F_{min} and F_{max} are the minimum and maximum X-ray flux during the 2 years of observations, and σ_{min} and σ_{max} are the corresponding errors. We define a source to be a variable if $S > 3\sigma$. The 99 sources we found to be variable using this criteria are indicated with a "v" in Table 2. We note that 6 of the sources are excluded from this analysis as they were only observed once. Thus, the variable sources represent $\sim 50\%$ of the total. The minimum amount of variability found corresponds to a factor of 1.5.

We note that the fraction of variable sources depends upon the region of M31 considered. In the central $2' \times 2'$ region, 73% of the sources are variable, while this fraction drops to 58% and 39% in regions 2 and 3, respectively (see Table 7). One might worry that this apparent trend is an artifact of the variation in PSF and/or diffuse background with off axis angle. The average number of background counts per source in regions 1 and 2 is < 3, while in region 3 the average is 12. These background counts could mask small variations in source flux. In order to determine the effect of the variable PSF, we used MARX [5] to simulate this effect. The maximum and minimum intensity images of the 24 variable sources found in region 1 were re-projected to random positions within region 3. The observed background (with Poisson noise) was included. We then re-computed S for these sources, and find that the average change from the original numbers is $\sim 2\%$. This indicates

[5] http://space.mit.edu/ASC/MARX/

that the measurement of variability is robust, and gives us some assurance that the difference in variability between the three regions is real.

Previous observations may be consistent with this apparent trend. For example, by comparing *ROSAT* observations to *Einstein* observations made 10 years earlier, PFJ93 found that $\sim 42\%$ of the X-ray sources in the central $7.5'$ region were variable. By comparing two *XMM-Newton* observations separated by six months Osborne et al. (2001) found that $> 15\%$ of the sources in the central $30'$ were variable.

We have also discovered 13 bright transients which are indicated with a "t" in Table 2. We define a bright transient as follows: i) the source has $S > 3\sigma$ *and* ii) the source is found in at least one observation with a luminosity of $\gtrsim 5 \times 10^{36}$ erg s^{-1} and is not detected in at least one of the other observations. The non-detection must be well above ($> 6\sigma$) the detection limit of the observation. Note that the luminosity limit covers typical outburst luminosities of soft X-ray transients and Be/X-ray binaries in our Galaxy.

One important transient was missed by this analysis because it had a peak luminosity below our "bright transient" threshold during the eight ACIS-I observations considered here. This object is XMMU J004234.1+411808 (= CXOM31 J004234.3+411809 = r2-29), which Osborne et al. (2001) and Trudolyubov, Borozdin, & Priedhorsky (2001) suggest is an X-ray nova. Observations with the HRC-I (OBSIDs 273, 275, and 276), the ACIS-S (OBSIDs 309 and 310) and XMM (Osborne et al. 2001) allow us to reconstruct the lightcurve (Figure 5), showing that this object had a peak $L_X \sim 2.4 \pm 0.5 \times 10^{37}$erg s^{-1} and an exponential decay with a ~ 20 day e-folding time. This source increases the number of bright transients discovered in the last two years within M31 to 14.

Two of these transients show typical lightcurves with a fast rise followed by an exponential decay (r2-29 and r2-28; see Figure 5) like those seen in our Galaxy (Chen, Shrader & Livio 1997). A different sort of behavior is shown by the transient discovered with *Chandra* in the first observation (Garcia et al. 2000a), which remained in outburst for more than one year and finally turned off in 2001 June (Figure 5). We note that Figure 5 includes data from the HRC-I and ACIS-S which we do not analyze herein beyond measuring counting rates and luminosities for these few sources. The temporal variability of the 14 transients and other sources will be described on a future paper which will fully utilize the HRC and ACIS data (Kong et al., in preparation).

One source, while not a bright transient, deserves special mention because of it's unusual long-term variability. Source r3-44 (Figure 5) is in the M31 globular cluster Bo86 and shows a possible ~ 200 day modulation. This is reminiscent of the Galactic source 4U 1820–30 in the globular cluster NGC 6624, which has a 176-d long-term modulation (e.g. Bloser et al. 2000).

3.6. X-ray Spectra and Spectral Variability

We extracted the energy spectra of the brightest 20 sources from the first observation (OBSID 303) and fit them to simple one-component models consisting of absorbed power-law, blackbody and Raymond-Smith (RS) shapes. In this paper we limit ourselves to the spectra as seen in this longest single observation (8.8 ks) because of the complications involved in fitting the spectrum of a source which appears at different detector positions and is observed at differing ACIS temperatures (i.e., with differing detector response matrices). These brightest 20 sources all have > 300 detected counts, and are well distributed across the field. They range from within $\sim 20''$ of the nucleus to over $7'$ distant. Circular extraction regions centered on the source positions were applied and correspond to 90% encircled energy. In order to employ χ^2 statistics to be used, all spectra were grouped into at least 20 counts per spectral bin.

All the sources were satisfactorily fit with simple absorbed power-law or RS models. Blackbody models gave very poor fits ($\chi^2_\nu > 2$) in most cases, except for sources r3-42, r3-52 and r3-61. Table 8 lists the best fitting parameters determined by the power-law and RS fits to these 20 sources. Except for r2-26 which suffers about 20% of pile-up, pile-up can be ignored for other sources. Pile-up will cause the energy spectrum harder than expected and we therefore extract the spectrum of r2-26 with an annulus region around the source (as the core is heavily affected by pile-up). The photon index softens to 1.6 comparing to $\alpha = 1$ before pile-up correction (see Table 8), suggesting pile-up affects the energy spectrum. Fitting the piled-up spectrum with pile-up model developed by Davies (2001) shows that both results are in good agreement. In addition, a high S/N spectrum obtained by *XMM-Newton* also shows similar results, confirming that the correct spectrum of r2-26 is very typical among M31 X-ray sources. The power-law photon indices of the 20 sources range from 1 to 3 with a mean of 1.8. The average and minimum RS temperatures (kT$\sim$ 16 keV and kT$>$ 2.4 keV, respectively) are both higher than that of coronal sources (Dempsey et al. 1993), indicating that none of these 20 sources is likely associated with a foreground star.

The column densities range from effectively zero to 9×10^{21} cm^{-2} and has an average value of $N_H = 2 \times 10^{21}$cm^{-2}. The Galactic absorption along the line of sight to M31 is $\sim 7 \times 10^{20}$cm^{-2} (Dickey & Lockman 1990), indicating that most of these bright sources have some additional local absorption. Figure 6 shows the spectra of the softest ($\alpha = 3$) and the hardest ($\alpha = 1.1$) X-ray sources among these 20 brightest objects.

We searched for spectral variability in all of the sources using a method analogous to that described in §3.5, but replacing F in equation (1) with HR2. If this newly defined S is greater than 3σ, the source is identified as a spectral variable and noted as "sv" in Table 2.

Only 12 sources are found to meet our criteria for spectral variability, corresponding to 6% of the total population. This is of course a lower limit, as small changes in the spectra of weak sources are undetectable with the number of counts accumulated in our 40 ks of merged data.

In order to further investigate the nature of the spectral variations, we fit simple spectra to two

of the brighter spectral variables. The fits show that as the counting rate increases, the spectrum becomes harder (see Figure 7). This is reminiscent of atoll and Z sources in our Galaxy (see e.g. Hasinger & van dar Klis 1989). The luminosity of these two sources ranges from $(0.4-1.0)\times10^{38}$ erg s^{-1}, which is higher than the typical luminosity of atoll sources ($<10^{37}$ erg s^{-1}). However, this luminosity is similar to that of the Z sources, which are believed to reach the Eddington limit (Psaltis, Lamb, & Miller 1995). The luminosity and spectral changes appear consistent with that seen in Z sources as they move along the "normal branch". These are probably the first extragalactic Z sources to be identified, except for LMC X–2 (Smale & Kuulkers 2000). Continued monitoring may confirm the nature of these sources by revealing the full Z-shape of the spectral variations observed for galactic Z sources.

4. Luminosity Function

The count rates for sources were converted into unabsorbed 0.3–7.0 keV luminosities by assuming an absorbed power-law model with $N_H = 10^{21}$ cm^{-2} and $\alpha = 1.7$. This is a median spectrum, as can be seen from Figure 3. The resulting conversion between count rate and luminosity is 7.5×10^{38} erg count^{-1}. Luminosities using this conversion are listed in Table 2. The derived luminosities are not very sensitive to the assumed spectral parameters, for example varying N_H from $(5-15)\times10^{21}$ cm^{-2} and α from 1.2 to 2.0 results in a $\sim20\%$ change in the conversion factor. An upper limit to the error in this conversion factor might be that found by using the thermal bremsstrahlung model of PFJ93, which gave luminosity differences up to 80%. For the brightest 20 X-ray sources, we derived the 0.3–7.0 keV luminosity directly from spectral fits (see §3.6).

In Figure 8 we plot the cumulative luminosity function (CLF) for all detected sources in the stacked image, and also plot separately the CLFs of the inner bulge (region 1), outer bulge (region 2), disk (region 3), and bulge (regions 1+2 combined). Histograms of the number of sources detected against S/N peak at S/N= 3.5 and fall off below this. Clearly we are incomplete below this level, and therefore limit our measurements of the LFs to sources with S/N> 3.5. We fitted a broken power-law model to the CLFs using standard χ^2 minimization techniques and found the slopes listed in Table 9. The CLF for all sources has a break at $(1.69\pm0.24)\times10^{37}$ erg s^{-1}, with $\alpha_1 = 0.38\pm0.01$ before the break and $\alpha_2 = 1.63\pm0.2$ after the break. This result is in good agreement with previous *ROSAT* (PFJ93) and *XMM-Newton* (Shirey et al. 2001) measurements of the CLF.

The CLF for the inner bulge is significantly different, with a break at a lower luminosity ($\sim1.5\times10^{36}$) and a significantly flatter distribution at the faint end. We performed a two-sample Kolmogorov-Smirnov (K-S) test for the luminosity functions of regions 1 and 3 and found that there is only a 3% probability that they are drawn from the same distribution.

In order to test if the flattening of the CLF of the inner bulge is due to incompleteness, we performed simulations using MARX. We assumed that the luminosity function of the sources in

the inner bulge is a *single* power-law that matches the best-fit function above the break ($\alpha = 0.7$) and extends to the faint end, and we generated sources at random positions and luminosities which conformed to this distribution. The diffuse emission (and background) were modeled by taking out all the detected sources, smoothing with a Gaussian and adding Poisson noise. The sources in the simulated observation were detected using the identical method used previously. Detected source counts were converted to luminosity using the same conversion factor. We found that the luminosity function did not show flattening below $\sim 10^{36}$ erg s^{-1}. A K-S test indicates that the simulated luminosity function is different from the actual one at a confidence level $> 99.99\%$ level. It is therefore likely that the flattening below the break is intrinsic and not due to incompleteness.

We determined the slopes for the CLFs (above) via minimum χ^2 fitting to these functions. However, the counts in a CLF are not independent and therefore this fitting method will underestimate the errors and may produce a biased best estimate of the slope. In order to more accurately estimate the errors and slopes, we used a maximum likelihood method (e.g. Crawford, Jauncey & Murdoch 1970) to determine the slopes in the differential luminosity functions (DLFs). The slopes determined by this method are shown in Table 9, where we have added one to the differential slopes in order to convert them into the equivalent cumulative slopes.

The slopes above the break seem insensitive to the analysis method. However at the faint end of the LF, below the apparent breaks, the two methods sometimes yield significantly different slopes. This is particularly true in the inner bulge region, where the maximum likelihood method indicates a much smaller change in slope that we found by χ^2 fitting to the CLF. While the appearance of the LFs (Figure 8) and the results of our MARX simulation (above) indicate the presence of a break to a flatter LF at the lowest fluxes, the maximum likelihood method suggests that the statistics in the inner bulge region are insufficient to either confirm the presence or constrain the size of a break. However, there are sufficient counts in the full catalog and in the disk region alone to confirm the changes in slope using the maximum likelihood method.

The black holes and neutron stars that power many of the M31 X-ray sources have formed through the evolution of initially massive stars. Because of this, the X-ray LF traces the history of star formation and evolution of these massive stars in binary systems. Breaks in the LF may indicate indicate an impulsive star formation event. As the X-ray binaries age, their average luminosity shifts to lower values and therefore the location of the break may be an indication of how long ago the star formation event occurred (Wu et al. 2002, Kilgard et al. 2002). Luminosity functions which do not show a break may indicate that star formation is still occurring. Chandra observations have measured the breaks in the LFs of several nearby galaxies, e.g. M81 (Tennant et al. 2001), NGC 1553 (Blanton, Sarazin, & Irwin 2001), NGC 4697 (Sarazin, Irwin, & Bregman 2001) and M83 (Soria & Wu 2002), and these breaks have been interpreted as evidence for impulsive star formation. Within M31, we find that the LF of three regions we studied has a break at a different luminosity. The inner bulge has this break at the lowest luminosity, and the luminosity of the break increases monotonically as we go out from the inner bulge. If the breaks do indicate the epochs of star formation events, then these events occurred most recently in the disk of M31 and further

back in time as we move towards the nucleus of M31.

As well as the monotonic shift in the break luminosity, there is a monotonic shift in the slopes of the LFs. As we move in towards the nucleus these slopes become progressively flatter. This is somewhat difficult to understand in the context of the discussion above, because the most luminous sources would be expected to have the shortest lifetimes. Loss of these sources as they age would tend to steepen the luminosity function, but we find flatter luminosity functions in the apparently older populations.

It is interesting to compare the LF of these three regions of M31 to those of other galaxies. M31 is not the first galaxy found to show a break in its LF nor is it the first to show different LFs in different regions; both M81 (Tennant et al. 2001) and M83 (Soria & Wu 2002) show similar behavior. In cases where a single slope is fit to the LF (i.e., where there is no clear break) the LFs of early type galaxies and the bulges of spirals tend to be steeper ($\alpha \sim 1.7$) than those of spiral disks and galaxies with active star forming regions ($\alpha \sim 0.8$, e.g, Prestwich 2001, Kilgard et al. 2002). The opposite seems to be the case within M31: the disk has a steeper LF than the bulge region. We speculate that this difference may be related to the location of the breaks in the M31 LF, which are at a somewhat lower luminosity than those seen in other galaxies. At these lower luminosities we may be sampling a different class of source, and the steepness of the LF may be due to inclusion of this new class of faint sources rather than a loss of bright sources. We note that there is some evidence that we are sampling a different class of sources as we move out from the bulge because the fraction of sources which show variability decreases monotonically. If these sources have an intrinsically steeper LF than bright accreting binaries, then they may be responsible for the steepening of the LFs as we move from the bulge towards the disk.

5. Summary

By using a stacked image (39.7 ks) of M31 from *Chandra* ACIS-I data taken between 1999 and 2001, we have detected 204 X-ray sources in the central $\sim 17' \times 17'$ region of M31, with luminosity above $\sim 1.6 \times 10^{35}$ erg s^{-1}. Of these 204 sources, we identified 21 globular clusters, 2 supernova remnants, 8 planetary nebula, 11 SSSs and 1 background object. We suggest that an additional 5 source are normal stars based on both their positional coincidence and soft spectra, and another ~ 30 sources may be background AGN based on deep field observations and their hard (possibly absorbed) spectra. We do not detect any OB associations or stellar nova.

We find 10 positional matches with M31 planetary nebular, but expect that ~ 2 of these may be random coincidences. The X-ray luminosity of these sources is an astounding 5 to 7 orders of magnitude higher than planetary nebula in the Galaxy. We suggest that these may not be planetary nebula at all, but analogs to GX 1+4 (i.e., symbiotic stars with a neutron star primary). Optical spectroscopy of these sources could confirm or refute this suggestion.

About 50% of all the detected sources are variable on time scales of months. We also found

14 transients, corresponding to $\sim 7\%$ of the total population. These transients show a variety of lightcurves, including the classical "FRED" (fast rise and exponential decay) with an e-folding decay time of ~ 30 days, an outburst lasting > 1 year, and a possible periodicity of ~ 200 days in one case. The first of these behaviors is analogous to X-ray nova in our Galaxy, the last reminiscent of the Galactic globular cluster source 4U 1820-30.

The median energy spectrum of point sources can be represented by a single power-law with a photon index of ~ 1.7. There are 11 sources with hardness ratios indicative of SSSs. The spectra of 12 sources are shown to be variable. The spectral variations and luminosity of the brightest of these sources is reminiscent of Galactic Z sources on the normal branch.

The luminosity function of all the X-ray point sources is consistent with the findings of *ROSAT* and *XMM-Newton* observations (PFJ93, Su97 and Shirey et al. 2001), with a break at $\sim 1.7 \times 10^{37}$ erg s^{-1} above which the function steepens. We also found that the luminosity functions of three separate regions (roughly corresponding to the inner bulge, outer bulge and disk) are different. In particular, the inner bulge shows a break near 10^{36} erg s^{-1}and it shifts monotonically to higher luminosities when moving outward from the nucleus to the outer bulge and disk. In addition, the slopes become steeper, indicating that the star formation and evolution histories might be different for the bulge and disk sources. Hence, our *Chandra* observations reveal different star formation histories even within the central $\sim 17' \times 17'$ (~ 3.9 kpc) region of M31. Future *Chandra* and *XMM-Newton* observations along the disk will definitely improve our knowledge of the star formation history of the whole galaxy.

We are grateful to Kinwah Wu, Andrea Prestwich and Phil Kaaret for stimulating discussion and comments. AKHK was supported by a Croucher Fellowship. MRG acknowledges the support of NASA LTSA Grant NAG5-10889 and NASA Contract NAS8-39073 to the CXC. The HRC GTO program is supported by NASA Contract NAS-38248. This research has made use of the SIMBAD database, operated at CDS, Strasbourg, France, and the NASA/IPAC Extragalactic Database (NED) which is operated by the Jet Propulsion Laboratory, Caltech, under contract with NASA.

REFERENCES

Barmby, P. 2001, PhD thesis, Harvard Univ

Battistini, P., Bonoli, F., Braccesi, A. Federici, L., Fusi Pecci F., Marano, B., & Borngen, F. 1987, A&AS, 67, 447

Berghofer, T.W., Schmitt, J.H.M.M., Danner, R., & Cassinelli, J.P. 1997, A&A 322, 167

Blanton, E.L., Sarazin, C.L., & Irwin, J.A. 2001, ApJ, 552, 106

Bloser, P.F., Grindlay, J.E., Kaaret, P., Zhang, W., Smale, A.P., & Barret, D. 2000, ApJ, 542, 1000

Brandt, W.N., et al. 2001, AJ, 122, 2810

Braun, R., & Walterbos, R.A.M. 1993, A&AS, 98, 327

Chen, W, Shrader, C.R., & Livio, M. 1997, ApJ, 491, 312

Ciardullo, R., Jacoby, G.H., Ford, H.C., & Neill, J.D. 1989 ApJ 339, 53

Crawford, D.F., Jauncey, D.L., & Murdoch, H.S. 1970, ApJ, 162, 405

Davies, J.E. 2001, ApJ, 562, 575

Dempsey, R.C., Linsky, J.L., Schmitt, J.H.M.M., & Fleming, T.A. 1993, ApJ, 413, 333

Dickey, J.M., & Lockman, F.J. 1990, ARA&A, 28, 215

Di Stefano, R., Kong, A.K.H., Garcia, M.R., Barmby, P., Greiner, J., Murray, S.S., & Primini, F.A. 2002, ApJ, in press (astro-ph/0106254)

d'Odorico, S., Dopita, M.A., & Benvenuti, P. 1980, A&AS, 40, 67

Donato, L., Garzia, S., Gonano, V., & Sostero, G. 2000 IAUC 7516

Dosaj, A. , Garcia, M.R., Forman, W. Jones, C., Kong, A., DiStefano, R., Primini, F.A., & Murray, S.S. 2001 in Proceedings "The High Energy Universe in Sharp Focus", in press, ASP, eds. S. Vrtilek, E.M. Schegel & L. Kuhi

Fiaschi, M., Di Mille, F., & Cariolato, R. 2001 IAUC 7709

Filippenko, A.V., Chornock, R.T., Coil, A.L., Leonard, D.C., & Li W.D. 2000 IAUC 7272

Ford, H.C. & Jacoby, G. 1978 ApJ, 219, 437

Freeman, P.E., Kashyap, V., Rosner, R., & Lamb, D.Q. 2002 ApJS, 138, 185

Garcia, M.R., Murray, S.S., Primini, F.A., Forman, W.R., McClintock, J.E. & Jones, C. 2000a, ApJ, 537, L23

Garcia, M.R., Murray, S.S., Primini, F.A., McClintock, J.E., & Callanan, P.J. 2000b, IAUC 7498

Garcia, M.R., Murray, S.S., Primini, F.A., Forman, W.R., Jones, C., & McClintock, J.E. 2001a, in proceeding of IAU205, Galaxies at the Highest Angular Resolution (astro-ph/0012387)

Garcia, M., Kong, A., Primini, F., McClintock, J., Murray, S., & Distefano, R. 2001b, ATel, 79

Garcia, M.R, et al. 2002, in preparation

Guerrero, M.A., Chu, Y.-H., Gruendl, R.A., Williams, R.M., & Kaler, J.B. 2001, ApJ, 553, L55

Guerrero, M.A., Chu, Y.-H., & Gruendl, R.A. 2000, ApJS, 129, 295

Johnson, R., Modjaz, M., & Li, W.D. 1999 IAUC 7236

Haiman, Z., et al. 1994, A&A, 286, 725

Hasinger, G., & van der Klis, M. 1989, A&A, 225, 79

Hornschemeier, A.E., et al. 2001, ApJ, 554, 742

Kahabka, P. 1999, A&A, 344, 459

Kastner, J.H., Vrtilek, S.D., Soker, N. 2001, ApJ, 550, L189

Kilgard, R.E., Kaaret, P., Krauss M.I., Prestwich A.H., Raley, M.T., Zezas, A. 2002, ApJ, submitted

Kong, A., Garcia, M., Murray, S., Primini, F., McClintock, J., & Di Stefano, R. 2001, ATel 76

Kong, A.K.H., Garcia, M.R., Primini, F.A., Di Stefano, R., Murray, S.S. 2002, in the Proceedings of the Symposium "New Visions of the X-ray Universe in the XMM-Newton and Chandra Era", 26-30 November 2001, ESTEC, The Netherlands (ESA SP-488). (astro-ph/0202065)

Li, W.D. 2000, IAUC 7477

Macri, L.M., et al. 2001, ApJ, 549, 721

Magnier, E.A. 1993, PhD Thesis, Massachusetts Institute of Technology

Magnier, E.A., Prins, S., van Paradijs, J., Lewin, W.H.G., Supper, R., Hasinger, G., Pietsch, W., & Truemper, J. 1995, A&AS, 114, 215

Magnier, E.A., Battinelli, P., Lewin, W. H. G., Haiman, Z., van Paradijs, J., Hasinger, G., Pietsch, W., Supper, R., & Truemper, J. 1993 A&A, 278, 36

Modjaz, M., & Li, W.D. 1999 IAUC 7218

Morton, D.C., Andereck, C.D., & Bernard, D.A. 1977, ApJ, 212, 13

Osborne, J.P., et al. 2001, A&A, 378, 800

Prestwich, A.H. 2001, in Proceedings "The High Energy Universe in Sharp Focus", in press, ASP, eds. S. Vrtilek, E.M. Schegel & L. Kuhi (astro-ph/0108523)

Primini, F., Garcia, M., Murray, S., Forman, W., Jones, C., & McClintock, J. 2000, in proceedings 232 WE-Heraeus Seminar, 22-25 May 2000, Bad Honnef, Germany. Edited by Elly M. Berkhuijsen, Rainer Beck, and Rene A. M. Walterbos. Shaker, Aachen, p. 145-148

Primini, F.A., Forman, W., & Jones, C. 1993, ApJ, 410, 615 (PFJ93)

Psaltis, D., Lamb, F.K., & Miller, G. S. 1995, ApJ, 454, L137

Sarazin, C.L., Irwin, J.A., & Bregman, J.N. 2001, ApJ, 556, 533

Shirey, R., et al. 2001, A&A, 365, L195

Shirey, R. 2001 IAUC 7659

Smale, A.P., & Kuulkers, E. 2000, ApJ, 528, 702

Stagni, R., Buonomo, U., & di Mille, F. 1999, IAUC 7093

Stanek, K.Z., & Garnavich, P.M. 1998, ApJ, 503, L131

Soria, R., & Wu, K. 2002, A&A, in press (astro-ph/0201059)

Supper, R., Hasinger, G., Pietsch, W., Trumper, J., Jain, A., Magnier, E.A., Lewin, W.H.G., & van Paradijs, J 1997, A&A, 317, 328 (Su97)

Supper, R., Hasinger, G., Lewin, W.H.G., Magnier, E.A., van Paradijs, J., Pietsch, W., Read, A.M., & Trumper, J. 2001. A&A, 373, 63 (Su01)

Tennant, A.F., Wu, K., Ghosh, K.K., Kolodziejczak, J.J., & Swartz, D.A. 2001, ApJ, 549, L43

Trinchieri, G., & Fabbiano, G. 1991, ApJ, 382, 82

Trudolyubov, S.P., Borozdin, K.N., Priedhorsky, W.C. 2001 ApJ, 563, L119

Wu, K., Tennant, A.F., Swartz, D.A., Ghosh, K.K., & Hunstead, R.W. 2001, ApJ, submitted

Table 1. Journal of *Chandra* Observations

Date	Obs ID	Exposure time (s)
Oct 13 1999	303	8830
Dec 11 1999	305	4129
Dec 27 1999	306	4132
Jan 29 2000	307	4113
Feb 16 2000	308	4012
Jul 29 2000	311	4894
Aug 27 2000	312	4666
Jun 10 2001	1583	4903

Table 2. *Chandra* ACIS catalog of the central region of M31

ID	IAU Name (CXOM31)	R.A. (h:m:s)	Dec. (°:′:″)	Positional Error (″)	Net Counts	Count Rate (10^{-2} s^{-1})	HR1 [a]
r3-110	J004150.2+411337	00:41:50.258	+41:13:37.16	1.7	91	0.22 ± 0.02	0.74 ± 0.43
r3-109	J004150.4+412114	00:41:50.436	+41:21:14.66	1.8	93	0.24 ± 0.03	0.45 ± 0.42
r3-81	J004151.5+411438	00:41:51.504	+41:14:38.29	1.1	164	0.41 ± 0.03	0.70 ± 0.26
r3-108	J004154.9+412303	00:41:54.932	+41:23:03.49	1.3	148	0.37 ± 0.04	0.80 ± 0.41
r3-62	J004204.0+411531	00:42:04.005	+41:15:31.97	0.6	81	0.20 ± 0.02	0.72 ± 0.19
r3-107	J004204.3+410930	00:42:04.357	+41:09:30.63	1.7	75	0.19 ± 0.03	0.40 ± 0.32
r3-80	J004205.6+411133	00:42:05.632	+41:11:33.87	1.1	45	0.11 ± 0.02	0.87 ± 0.36
r3-79	J004207.0+411719	00:42:07.019	+41:17:19.17	0.6	44	0.11 ± 0.02	0.88 ± 0.34
r3-94	J004207.4+411025	00:42:07.422	+41:10:25.63	1.0	71	0.18 ± 0.02	0.50 ± 0.27
r3-61	J004207.6+411815	00:42:07.619	+41:18:15.17	0.1	1611	4.06 ± 0.10	0.62 ± 0.04
r3-93	J004208.2+411250	00:42:08.200	+41:12:50.92	1.0	32	0.08 ± 0.02	1.00 ± 0.46
r3-60	J004208.9+412048	00:42:08.952	+41:20:48.42	0.3	435	1.10 ± 0.05	0.73 ± 0.09
r3-59	J004209.3+411745	00:42:09.372	+41:17:45.63	0.2	443	1.12 ± 0.05	0.66 ± 0.07
r3-102	J004209.6+412008	00:42:09.614	+41:20:08.89	1.0	19	0.05 ± 0.01	1.00 ± 0.49
r3-58	J004210.1+411509	00:42:10.164	+41:15:09.90	0.3	148	0.37 ± 0.03	0.52 ± 0.12
r3-57	J004210.8+411248	00:42:10.839	+41:12:48.05	0.4	123	0.31 ± 0.03	0.11 ± 0.12
r3-78	J004210.9+410646	00:42:10.954	+41:06:46.95	1.3	213	0.54 ± 0.04	0.09 ± 0.19
r3-56	J004211.6+411048	00:42:11.633	+41:10:48.70	0.4	295	0.74 ± 0.04	0.61 ± 0.12
r3-55	J004211.8+411648	00:42:11.866	+41:16:48.49	0.3	154	0.39 ± 0.03	0.85 ± 0.15
r3-54	J004212.0+411758	00:42:12.026	+41:17:58.86	0.1	538	1.36 ± 0.06	0.72 ± 0.07
r3-92	J004212.6+411244	00:42:12.670	+41:12:44.79	1.0	20	0.05 ± 0.01	1.00 ± 0.58
r3-53	J004212.9+411628	00:42:12.944	+41:16:28.18	0.6	30	0.07 ± 0.01	0.48 ± 0.24
r3-52	J004213.0+411836	00:42:13.017	+41:18:36.73	0.1	2805	7.07 ± 0.13	0.72 ± 0.03
r3-77	J004214.1+412105	00:42:14.195	+41:21:05.82	0.7	13	0.03 ± 0.01	-0.83 ± 0.60
r3-51	J004214.9+412122	00:42:14.951	+41:21:22.04	0.6	15	0.04 ± 0.01	-0.37 ± 0.50
r3-50	J004215.0+411234	00:42:15.011	+41:12:34.23	0.1	1017	2.56 ± 0.08	0.43 ± 0.04
r3-49	J004215.1+411802	00:42:15.138	+41:18:02.25	0.5	81	0.20 ± 0.02	0.82 ± 0.18
r3-48	J004215.3+412032	00:42:15.350	+41:20:32.27	0.3	205	0.52 ± 0.04	0.57 ± 0.10
r3-47	J004215.5+411721	00:42:15.571	+41:17:21.11	0.1	783	1.97 ± 0.07	0.54 ± 0.05
r3-106	J004215.6+412216	00:42:15.694	+41:22:16.18	1.4	21	0.05 ± 0.01	0.73 ± 0.54
r3-76	J004215.9+411552	00:42:15.988	+41:15:52.91	0.6	16	0.04 ± 0.01	0.26 ± 0.63
r3-75	J004216.4+411610	00:42:16.462	+41:16:10.55	0.7	15	0.04 ± 0.01	0.37 ± 0.39

Table 2—Continued

ID	IAU Name (CXOM31)	R.A. (h:m:s)	Dec. (°:′:″)	Positional Error (″)	Net Counts	Count Rate (10^{-2} s^{-1})	HR1 [a]	
r3-91	J004216.8+411856	00:42:16.808	+41:18:56.89	1.0	17	0.04 ± 0.01	0.45 ± 0.39	
r3-46	J004216.9+411508	00:42:16.919	+41:15:08.54	0.3	114	0.29 ± 0.03	0.70 ± 0.16	
r3-45	J004218.2+411223	00:42:18.241	+41:12:23.53	0.1	2011	5.07 ± 0.11	0.38 ± 0.03	-
r3-44	J004218.5+411401	00:42:18.534	+41:14:01.69	0.1	2428	6.12 ± 0.12	0.43 ± 0.03	
r3-90	J004218.8+412004	00:42:18.859	+41:20:04.38	0.7	17	0.04 ± 0.01	0.68 ± 0.38	
r3-74	J004219.5+412154	00:42:19.579	+41:21:54.07	0.7	38	0.10 ± 0.02	1.00 ± 0.50	
r3-89	J004220.2+411313	00:42:20.235	+41:13:13.98	0.8	15	0.04 ± 0.01	0.51 ± 0.46	-
r3-101	J004220.2+410824	00:42:20.290	+41:08:24.78	1.4	34	0.09 ± 0.02	0.12 ± 0.33	
r3-43	J004220.9+411808	00:42:20.997	+41:18:08.55	0.3	88	0.22 ± 0.02	0.81 ± 0.16	
r3-42	J004221.3+411601	00:42:21.382	+41:16:01.32	0.1	1447	3.65 ± 0.10	0.61 ± 0.04	
r3-41	J004221.4+411419	00:42:21.435	+41:14:19.54	0.2	155	0.39 ± 0.03	0.23 ± 0.10	-
r3-40	J004222.3+411333	00:42:22.316	+41:13:33.99	0.1	986	2.49 ± 0.08	0.39 ± 0.04	
r3-88	J004222.5+412234	00:42:22.541	+41:22:34.92	0.9	31	0.08 ± 0.02	0.09 ± 0.28	
r3-39	J004222.8+411535	00:42:22.841	+41:15:35.14	0.04	2959	7.46 ± 0.14	0.50 ± 0.03	
r3-73	J004222.8+410738	00:42:22.880	+41:07:38.21	0.8	129	0.33 ± 0.03	0.40 ± 0.18	
r3-38	J004223.0+411407	00:42:23.047	+41:14:07.49	0.1	699	1.76 ± 0.07	0.43 ± 0.05	
r2-57	J004224.0+411733	00:42:24.079	+41:17:33.58	0.4	16	0.04 ± 0.01	-0.84 ± 0.43	-
r2-52	J004224.1+411535	00:42:24.109	+41:15:35.84	0.3	27	0.07 ± 0.01	-0.16 ± 0.24	-
r2-45	J004225.0+411340	00:42:25.034	+41:13:40.40	0.1	207	0.52 ± 0.04	0.19 ± 0.09	-
r2-36	J004225.9+411915	00:42:25.941	+41:19:15.27	0.1	494	1.25 ± 0.06	0.48 ± 0.06	
r3-87	J004226.0+412552	00:42:26.047	+41:25:52.74	1.0	431	1.09 ± 0.05	0.62 ± 0.25	
r3-37	J004227.5+412048	00:42:27.541	+41:20:48.69	0.7	25	0.06 ± 0.01	0.20 ± 0.30	
r3-36	J004228.0+410959	00:42:28.089	+41:09:59.84	0.1	1170	2.95 ± 0.09	0.48 ± 0.04	
r2-35	J004228.1+411222	00:42:28.190	+41:12:22.76	0.04	2865	7.22 ± 0.14	0.43 ± 0.03	
r3-111	J004228.7+410434	00:42:28.789	+41:04:34.98	1.0	1783	4.49 ± 0.11	0.64 ± 0.09	
r2-44	J004230.1+411653	00:42:30.166	+41:16:53.41	0.2	15	0.04 ± 0.01	0.70 ± 0.47	
r2-43	J004230.8+411910	00:42:30.865	+41:19:10.32	0.2	32	0.08 ± 0.01	0.41 ± 0.22	
r2-34	J004231.0+411621	00:42:31.045	+41:16:21.74	0.02	2409	6.07 ± 0.12	0.44 ± 0.03	
r2-33	J004231.1+411939	00:42:31.154	+41:19:39.19	0.1	608	1.53 ± 0.06	0.53 ± 0.06	
r2-51	J004231.1+412008	00:42:31.193	+41:20:08.30	0.3	25	0.06 ± 0.01	0.42 ± 0.29	
r3-86	J004231.8+412306	00:42:31.898	+41:23:06.19	1.0	27	0.07 ± 0.02	0.99 ± 0.48	
r2-32	J004231.9+411314	00:42:31.979	+41:13:14.24	0.04	1487	3.75 ± 0.10	0.22 ± 0.03	

Table 2—Continued

ID	IAU Name (CXOM31)	R.A. (h:m:s)	Dec. (°:′:″)	Positional Error (″)	Net Counts	Count Rate (10^{-2} s^{-1})	HR1 [a]
r2-55	J004232.4+411545	00:42:32.437	+41:15:45.62	0.3	12	0.03 ± 0.01	0.85 ± 0.79
r2-31	J004232.6+411310	00:42:32.648	+41:13:10.77	0.1	306	0.77 ± 0.04	0.44 ± 0.08
r2-30	J004233.8+411619	00:42:33.806	+41:16:19.88	0.05	362	0.91 ± 0.05	0.36 ± 0.07
r3-35	J004234.0+412150	00:42:34.069	+41:21:50.23	0.3	134	0.34 ± 0.03	0.77 ± 0.16
r2-29	J004234.3+411809	00:42:34.361	+41:18:09.60	0.1	39	0.10 ± 0.02	0.27 ± 0.21
r2-28	J004234.6+411523	00:42:34.693	+41:15:23.32	0.1	165	0.42 ± 0.03	0.16 ± 0.09
r2-27	J004235.1+412006	00:42:35.121	+41:20:06.09	0.1	385	0.97 ± 0.05	0.63 ± 0.09
r2-42	J004236.5+411350	00:42:36.514	+41:13:50.20	0.2	39	0.10 ± 0.02	-0.14 ± 0.16
r3-100	J004237.8+410526	00:42:37.862	+41:05:26.07	1.8	69	0.17 ± 0.03	0.65 ± 0.37
r2-26	J004238.5+411603	00:42:38.503	+41:16:03.80	0.01	7749	19.53 ± 0.22	0.53 ± 0.02
r2-54	J004238.6+411526	00:42:38.692	+41:15:26.44	0.3	12	0.03 ± 0.01	0.07 ± 0.39
r2-25	J004239.4+411428	00:42:39.451	+41:14:28.52	0.1	287	0.72 ± 0.04	0.35 ± 0.07
r1-15	J004239.9+411547	00:42:39.908	+41:15:47.68	0.02	1100	2.77 ± 0.08	0.29 ± 0.04
r2-24	J004240.1+411845	00:42:40.121	+41:18:45.38	0.1	316	0.80 ± 0.05	0.48 ± 0.08
r2-23	J004240.4+411355	00:42:40.446	+41:13:55.33	0.1	18	0.05 ± 0.01	0.62 ± 0.40
r2-22	J004240.5+411327	00:42:40.566	+41:13:27.30	0.04	716	1.81 ± 0.07	0.39 ± 0.05
r3-34	J004240.6+411032	00:42:40.610	+41:10:32.32	0.5	74	0.19 ± 0.02	0.37 ± 0.18
r3-33	J004240.8+412216	00:42:40.834	+41:22:16.58	0.7	22	0.06 ± 0.01	-0.33 ± 0.30
r3-85	J004240.9+410701	00:42:40.938	+41:07:01.24	1.1	31	0.08 ± 0.02	1.00 ± 0.51
r3-32	J004240.9+411101	00:42:40.983	+41:11:01.72	0.7	10	0.02 ± 0.01	1.00 ± 0.60
r1-32	J004241.3+411523	00:42:41.355	+41:15:23.94	0.1	130	0.33 ± 0.03	0.42 ± 0.14
r3-31	J004241.5+412106	00:42:41.566	+41:21:06.02	0.3	142	0.36 ± 0.03	0.52 ± 0.13
r1-31	J004241.9+411532	00:42:41.998	+41:15:32.18	0.1	90	0.23 ± 0.02	0.35 ± 0.14
r1-5	J004242.0+411608	00:42:42.082	+41:16:08.42	0.01	2779	7.00 ± 0.13	0.44 ± 0.03
r2-53	J004242.0+411914	00:42:42.093	+41:19:14.20	0.4	8	0.02 ± 0.01	1.00 ± 2.22
r2-21	J004242.2+411445	00:42:42.249	+41:14:45.54	0.05	545	1.37 ± 0.06	0.33 ± 0.06
r1-14	J004242.3+411553	00:42:42.386	+41:15:53.82	0.02	772	1.95 ± 0.07	0.43 ± 0.05
r1-30	J004242.4+411659	00:42:42.437	+41:16:59.59	0.1	70	0.18 ± 0.02	0.25 ± 0.16
r2-20	J004242.6+411455	00:42:42.632	+41:14:55.63	0.1	41	0.10 ± 0.02	-0.13 ± 0.21
r1-13	J004242.9+411543	00:42:42.907	+41:15:43.26	0.03	600	1.51 ± 0.06	0.43 ± 0.05
r3-99	J004242.9+410830	00:42:42.972	+41:08:30.48	1.1	24	0.06 ± 0.01	0.91 ± 0.58
r1-24	J004243.1+411640	00:42:43.114	+41:16:40.31	0.1	55	0.14 ± 0.02	0.43 ± 0.22

Table 2—Continued

ID	IAU Name (CXOM31)	R.A. (h:m:s)	Dec. (°:′:″)	Positional Error (″)	Net Counts	Count Rate (10^{-2} s^{-1})	HR1 [a]	
r2-19	J004243.2+411319	00:42:43.225	+41:13:19.48	0.1	166	0.42 ± 0.03	-0.30 ± 0.09	-0
r1-12	J004243.6+411632	00:42:43.661	+41:16:32.60	0.02	620	1.56 ± 0.06	0.39 ± 0.05	0
r1-28	J004243.7+411514	00:42:43.715	+41:15:14.54	0.1	16	0.04 ± 0.01	0.30 ± 0.41	0
r1-29	J004243.7+411629	00:42:43.718	+41:16:29.39	0.1	72	0.18 ± 0.02	0.30 ± 0.14	-0
r1-27	J004243.7+411611	00:42:43.770	+41:16:11.37	0.1	39	0.10 ± 0.02	0.37 ± 0.24	0
r1-23	J004243.7+411604	00:42:43.778	+41:16:04.05	0.04	174	0.44 ± 0.03	0.26 ± 0.09	-0
r1-11	J004243.8+411629	00:42:43.805	+41:16:29.97	0.03	273	0.69 ± 0.04	0.48 ± 0.08	0
r1-33	J004244.0+411604	00:42:44.001	+41:16:04.23	0.1	13	0.03 ± 0.01	-0.26 ± 0.31	-0
r1-22	J004244.2+411614	00:42:44.205	+41:16:14.25	0.1	71	0.18 ± 0.02	0.52 ± 0.17	0
r1-10	J004244.2+411608	00:42:44.273	+41:16:08.90	0.03	287	0.73 ± 0.04	0.11 ± 0.07	-0
r1-21	J004244.2+411605	00:42:44.277	+41:16:05.56	0.04	197	0.50 ± 0.04	0.32 ± 0.08	-0
r1-9	J004244.2+411607	00:42:44.287	+41:16:07.65	0.03	286	0.72 ± 0.04	-0.05 ± 0.06	-0
r3-30	J004244.3+411157	00:42:44.326	+41:11:57.90	0.2	209	0.53 ± 0.04	0.32 ± 0.09	0
r1-8	J004244.5+411618	00:42:44.589	+41:16:18.28	0.04	234	0.59 ± 0.04	0.12 ± 0.07	-0
r3-29	J004244.7+411137	00:42:44.766	+41:11:37.76	0.1	1306	3.29 ± 0.09	0.31 ± 0.03	-0
r2-18	J004244.8+411739	00:42:44.817	+41:17:39.82	0.1	185	0.47 ± 0.03	0.42 ± 0.10	0
r1-26	J004244.9+411523	00:42:44.995	+41:15:23.30	0.1	111	0.28 ± 0.03	0.17 ± 0.12	-0
r2-17	J004245.0+411407	00:42:45.014	+41:14:07.13	0.1	106	0.27 ± 0.03	0.29 ± 0.13	0
r1-4	J004245.0+411621	00:42:45.031	+41:16:21.90	0.02	908	2.29 ± 0.08	0.31 ± 0.04	0
r2-16	J004245.1+411722	00:42:45.141	+41:17:22.49	0.1	308	0.78 ± 0.04	0.41 ± 0.08	0
r1-20	J004245.1+411611	00:42:45.148	+41:16:11.31	0.1	125	0.32 ± 0.03	0.06 ± 0.10	-0
r1-7	J004245.5+411608	00:42:45.508	+41:16:08.79	0.04	164	0.41 ± 0.03	0.36 ± 0.10	0
r3-72	J004245.6+412434	00:42:45.673	+41:24:34.46	0.8	50	0.13 ± 0.02	0.19 ± 0.34	0
r1-19	J004245.9+411619	00:42:45.918	+41:16:19.77	0.1	105	0.26 ± 0.03	0.25 ± 0.12	-0
r2-15	J004245.9+411736	00:42:45.989	+41:17:36.35	0.1	48	0.12 ± 0.02	0.40 ± 0.22	0
r1-18	J004246.0+411543	00:42:46.066	+41:15:43.37	0.1	88	0.22 ± 0.02	0.47 ± 0.15	0
r3-28	J004246.8+412119	00:42:46.834	+41:21:19.65	0.3	79	0.20 ± 0.02	0.71 ± 0.20	0
r1-3	J004246.8+411615	00:42:46.885	+41:16:15.76	0.02	934	2.35 ± 0.08	0.39 ± 0.04	0
r1-2	J004247.0+411628	00:42:47.089	+41:16:28.65	0.01	2600	6.55 ± 0.13	0.49 ± 0.03	0
r3-27	J004247.1+411157	00:42:47.154	+41:11:57.75	0.3	84	0.21 ± 0.02	0.38 ± 0.15	0
r3-26	J004247.7+411052	00:42:47.785	+41:10:52.42	0.5	23	0.06 ± 0.01	0.58 ± 0.36	0
r1-17	J004247.7+411623	00:42:47.787	+41:16:23.19	0.05	138	0.35 ± 0.03	0.48 ± 0.11	0

Table 2—Continued

ID	IAU Name (CXOM31)	R.A. (h:m:s)	Dec. (°:′:″)	Positional Error (″)	Net Counts	Count Rate (10^{-2} s^{-1})	HR1 [a]	
r1-25	J004247.8+411549	00:42:47.810	+41:15:49.85	0.1	26	0.07 ± 0.01	-0.79 ± 0.28	−
r1-6	J004247.8+411533	00:42:47.813	+41:15:33.04	0.02	1002	2.53 ± 0.08	0.18 ± 0.04	−
r3-25	J004248.4+412523	00:42:48.423	+41:25:23.10	0.3	574	1.45 ± 0.06	0.60 ± 0.07	0
r1-1	J004248.4+411521	00:42:48.450	+41:15:21.31	0.01	3360	8.47 ± 0.15	0.42 ± 0.02	0
r1-16	J004248.6+411624	00:42:48.637	+41:16:24.64	0.05	144	0.36 ± 0.03	0.22 ± 0.10	−
r3-84	J004248.8+412406	00:42:48.892	+41:24:06.87	0.8	59	0.15 ± 0.02	-0.86 ± 0.21	−
r2-41	J004249.0+411742	00:42:49.063	+41:17:42.25	0.2	15	0.04 ± 0.01	-0.05 ± 0.33	−
r2-14	J004249.1+411816	00:42:49.155	+41:18:16.26	0.1	322	0.81 ± 0.05	0.45 ± 0.08	0
r3-98	J004249.3+410635	00:42:49.311	+41:06:35.69	1.1	37	0.09 ± 0.02	0.66 ± 0.40	−
r3-24	J004249.9+411108	00:42:49.913	+41:11:08.64	0.5	38	0.09 ± 0.02	0.14 ± 0.43	0
r2-40	J004250.1+411813	00:42:50.150	+41:18:13.11	0.3	11	0.03 ± 0.01	0.46 ± 0.54	0
r2-56	J004250.3+411556	00:42:50.398	+41:15:56.15	0.3	12	0.03 ± 0.01	-0.71 ± 0.48	−
r3-71	J004250.6+411033	00:42:50.654	+41:10:33.58	0.7	28	0.07 ± 0.01	-0.23 ± 0.28	−
r3-70	J004251.4+412633	00:42:51.461	+41:26:33.58	1.0	80	0.69 ± 0.08	0.30 ± 0.36	0
r2-39	J004251.5+411302	00:42:51.555	+41:13:02.65	0.2	46	0.12 ± 0.02	0.58 ± 0.23	0
r2-50	J004252.2+411735	00:42:52.203	+41:17:35.02	0.2	22	0.05 ± 0.01	0.53 ± 0.29	0
r2-49	J004252.4+411835	00:42:52.448	+41:18:35.24	0.3	12	0.03 ± 0.01	1.00 ± 0.81	1
r2-12	J004252.4+411540	00:42:52.450	+41:15:40.20	0.03	918	2.31 ± 0.08	-0.99 ± 0.05	−
r2-13	J004252.4+411854	00:42:52.450	+41:18:54.75	0.02	3943	9.94 ± 0.16	0.49 ± 0.02	0
r2-38	J004252.5+411328	00:42:52.543	+41:13:28.72	0.2	13	0.03 ± 0.01	0.09 ± 0.36	−
r3-69	J004253.5+412553	00:42:53.578	+41:25:53.56	0.7	188	0.47 ± 0.04	-0.43 ± 0.12	−
r2-11	J004254.8+411603	00:42:54.859	+41:16:03.46	0.02	3282	8.27 ± 0.14	0.42 ± 0.03	0
r2-10	J004255.1+411836	00:42:55.108	+41:18:36.33	0.1	179	0.45 ± 0.03	0.39 ± 0.09	−
r3-23	J004255.3+412556	00:42:55.316	+41:25:56.60	0.3	1011	2.55 ± 0.08	0.64 ± 0.08	0
r2-9	J004255.5+411835	00:42:55.550	+41:18:35.44	0.1	108	0.27 ± 0.03	0.26 ± 0.12	−
r2-8	J004256.8+411844	00:42:56.836	+41:18:44.37	0.1	286	0.72 ± 0.04	0.32 ± 0.07	0
r3-22	J004257.8+411104	00:42:57.854	+41:11:04.59	0.1	1646	4.15 ± 0.10	0.39 ± 0.03	0
r2-7	J004258.2+411529	00:42:58.257	+41:15:29.46	0.1	487	1.23 ± 0.06	0.36 ± 0.06	−
r2-59	J004258.5+411200	00:42:58.543	+41:12:00.14	0.6	15	0.04 ± 0.01	-0.23 ± 1.07	0
r2-58	J004259.0+411158	00:42:59.015	+41:11:58.75	0.6	14	0.03 ± 0.01	1.00 ± 0.71	1
r3-97	J004259.0+412613	00:42:59.082	+41:26:13.76	1.2	130	0.33 ± 0.03	0.70 ± 0.35	0
r2-48	J004259.4+411242	00:42:59.480	+41:12:42.26	0.3	41	0.10 ± 0.02	0.33 ± 0.23	0

Table 2—Continued

ID	IAU Name (CXOM31)	R.A. (h:m:s)	Dec. (°:′:″)	Positional Error (″)	Net Counts	Count Rate (10^{-2} s^{-1})	HR1 [a]
r2-6	J004259.5+411919	00:42:59.594	+41:19:19.72	0.04	1678	4.23 ± 0.10	0.38 ± 0.03
r2-5	J004259.8+411606	00:42:59.803	+41:16:06.01	0.03	1356	3.42 ± 0.09	0.43 ± 0.04
r2-37	J004301.0+411351	00:43:01.041	+41:13:51.69	0.2	65	0.16 ± 0.02	0.50 ± 0.17
r2-47	J004301.6+411814	00:43:01.638	+41:18:14.98	0.2	15	0.04 ± 0.01	0.41 ± 0.40
r3-96	J004301.6+411052	00:43:01.676	+41:10:52.63	0.8	15	0.04 ± 0.01	-0.40 ± 0.36
r2-46	J004301.7+411726	00:43:01.743	+41:17:26.78	0.3	12	0.03 ± 0.01	-0.32 ± 0.38
r3-68	J004302.3+411203	00:43:02.343	+41:12:03.71	0.9	17	0.04 ± 0.01	1.00 ± 0.71
r2-4	J004302.8+411522	00:43:02.877	+41:15:22.82	0.04	1430	3.60 ± 0.10	0.40 ± 0.03
r3-21	J004302.9+412042	00:43:02.958	+41:20:42.54	0.3	84	0.21 ± 0.02	0.84 ± 0.20
r3-20	J004303.0+411015	00:43:03.089	+41:10:15.18	0.2	284	0.72 ± 0.04	0.21 ± 0.08
r2-3	J004303.1+411528	00:43:03.163	+41:15:28.00	0.04	1249	3.15 ± 0.09	0.29 ± 0.03
r3-19	J004303.2+412122	00:43:03.231	+41:21:22.42	0.1	632	1.59 ± 0.06	0.33 ± 0.05
r2-2	J004303.8+411805	00:43:03.812	+41:18:05.23	0.05	1174	2.96 ± 0.09	0.41 ± 0.04
r2-1	J004304.1+411601	00:43:04.186	+41:16:01.62	0.1	249	0.63 ± 0.04	0.29 ± 0.08
r3-83	J004306.6+412243	00:43:06.618	+41:22:43.82	0.9	27	0.07 ± 0.02	0.50 ± 0.64
r3-67	J004306.7+411912	00:43:06.723	+41:19:12.26	0.6	32	0.08 ± 0.02	-0.02 ± 0.23
r3-18	J004307.4+412020	00:43:07.472	+41:20:20.09	0.2	195	0.49 ± 0.04	0.37 ± 0.10
r3-95	J004307.7+412418	00:43:07.738	+41:24:18.16	1.2	33	0.08 ± 0.02	-0.11 ± 0.39
r3-17	J004308.6+411248	00:43:08.609	+41:12:48.30	0.2	320	0.81 ± 0.05	0.51 ± 0.09
r3-16	J004309.7+411901	00:43:09.791	+41:19:01.22	0.2	396	1.00 ± 0.05	0.35 ± 0.06
r3-15	J004310.5+411451	00:43:10.587	+41:14:51.55	0.04	4432	11.17 ± 0.17	0.39 ± 0.02
r3-14	J004311.3+411809	00:43:11.313	+41:18:09.76	0.5	43	0.11 ± 0.02	1.00 ± 0.35
r3-13	J004313.1+411813	00:43:13.172	+41:18:13.96	0.3	103	0.26 ± 0.03	0.32 ± 0.13
r3-12	J004313.9+411712	00:43:13.908	+41:17:12.19	0.8	22	0.05 ± 0.01	0.19 ± 0.37
r3-112	J004314.2+410725	00:43:14.245	+41:07:25.42	0.8	1051	2.65 ± 0.08	0.87 ± 0.34
r3-11	J004314.2+411651	00:43:14.266	+41:16:51.31	0.6	42	0.11 ± 0.02	0.38 ± 0.21
r3-105	J004314.5+412513	00:43:14.507	+41:25:13.66	1.5	62	0.16 ± 0.02	0.62 ± 0.53
r3-10	J004315.4+411125	00:43:15.421	+41:11:25.00	0.6	77	0.19 ± 0.02	0.28 ± 0.16
r3-9	J004316.0+411841	00:43:16.087	+41:18:41.73	0.3	166	0.42 ± 0.03	0.52 ± 0.11
r3-8	J004318.7+412018	00:43:18.773	+41:20:18.52	0.6	85	0.21 ± 0.03	-0.96 ± 0.19
r3-66	J004320.8+411852	00:43:20.844	+41:18:52.62	0.7	18	0.04 ± 0.01	0.25 ± 0.34
r3-7	J004321.0+411751	00:43:21.058	+41:17:51.19	0.4	194	0.49 ± 0.04	0.35 ± 0.10

Table 2—Continued

ID	IAU Name (CXOM31)	R.A. (h:m:s)	Dec. (°:′:″)	Positional Error (″)	Net Counts	Count Rate (10^{-2} s^{-1})	HR1 [a]	
r3-104	J004321.4+411558	00:43:21.432	+41:15:58.34	1.0	19	0.05 ± 0.01	1.00 ± 0.49	
r3-82	J004322.2+411258	00:43:22.205	+41:12:58.67	1.0	16	0.04 ± 0.01	0.78 ± 0.63	
r3-65	J004324.0+411314	00:43:24.070	+41:13:14.34	0.9	28	0.07 ± 0.02	0.79 ± 0.55	
r3-6	J004324.8+411728	00:43:24.879	+41:17:28.33	0.5	101	0.25 ± 0.03	0.52 ± 0.17	
r3-5	J004325.9+411935	00:43:25.948	+41:19:35.88	0.4	34	0.08 ± 0.02	-0.34 ± 0.38	-
r3-4	J004326.2+411756	00:43:26.250	+41:17:56.87	0.8	22	0.05 ± 0.01	0.11 ± 0.40	-
r3-64	J004326.2+411910	00:43:26.298	+41:19:10.82	1.0	82	0.21 ± 0.03	0.65 ± 0.44	
r3-63	J004327.7+411829	00:43:27.763	+41:18:29.83	0.6	258	0.65 ± 0.04	-0.45 ± 0.12	-
r3-103	J004329.0+410749	00:43:29.038	+41:07:49.11	2.6	1387	3.49 ± 0.10	0.76 ± 0.23	
r3-3	J004332.3+411041	00:43:32.382	+41:10:41.66	0.4	1419	3.58 ± 0.10	0.80 ± 0.12	
r3-2	J004334.3+411323	00:43:34.332	+41:13:23.72	0.4	994	2.51 ± 0.08	0.38 ± 0.06	-
r3-1	J004337.1+411443	00:43:37.191	+41:14:43.07	0.4	2264	5.71 ± 0.12	0.55 ± 0.06	

[a]HR1 = (M–S)/(M+S)

[b]HR2 = (H–S)/(H+S)

[c]Luminosity in 0.3–7 keV (erg s^{-1})

Note. — e: Extragalactic objects; f: Foreground stars; g: GC; p: PN; r: *ROSAT* HRI sources; s: SNR; v: Va
t:transients

Table 3. Summary of Source IDs

Object type	Catalogs	Searching radius ($''$)	N_m	N_{acc}	N_{true}
X-ray	*ROSAT* HRI (PFJ93)	6	77	7.5	69
GC	Ba87, Magnier (1993), and Barmby (2001)	3	22	1.75	21
SNR	DO80, BW83, and Ma95	10	2	1.5	2
PN	Ford78, Ci89	3	10	2.5	8
OB Assoc.	Magnier et al. 1993	3	0	0.25	0
Nova	IAUC	3	0	0.25	0
Extragalactic	NED and SIMBAD	3	1	1	1
Stars	Ha94 and SIMBAD	1	40	34.75	5

Note. — N_m: Number of all possible matches; N_{acc}: Number of matches by accident; N_{final}: likely number of true matches.

References. — Ba87: Battistini et al. 1987; DO80: d'Odorico, Dopita, & Benvenuti (1980); BW83: Braun & Walterbos (1993); Ma95: Magnier et al. (1995); Ford78: Ford & Jacoby (1978); Ci89: Ciardullo et al. (1989); Ha94: Haiman et al. (1994)

Table 4. Optical IDs

My ref.	*Chandra* Name	Type	Identification	Offset (″)
r3-59	CXOM31 J004209.3+411745	GC	mita140	1.9
r3-54	CXOM31 J004212.0+411758	GC	Bo78,mita153	2.9,1.8
r3-44	CXOM31 J004218.5+411401	GC	Bo86	1.9
r3-74	CXOM31 J004219.5+412154	GC	mita165,166	1.1
r2-36	CXOM31 J004225.9+411915	GC	Bo96,mita174	2.5,1.9
r2-33	CXOM31 J004231.1+411939	GC	Bo107,mita192	1.7,1.5
r2-42	CXOM31 J004236.5+411350	Star	Ha94(238140)	1.0
r2-54	CXOM31 J004238.6+411526	Star	Ha94(247501)	0.8
r1-15	CXOM31 J004239.9+411547	PN	Ford17	2.1
r3-34	CXOM31 J004240.6+411032	GC	mita212	1.0
r3-33	CXOM31 J004240.8+412216	Star	Ha94(278717)	0.7
r1-32	CXOM31 J004241.3+411523	GC	mita213	2.3
r1-24	CXOM31 J004243.1+411640	PN	Ford322	0.9
r1-21	CXOM31 J004244.2+411605	PN	Ford316	2.4
r1-33	CXOM31 J004244.0+411604			2.4
r1-26	CXOM31 J004244.9+411523	PN	Ford21,74	1.6,2.9
r2-15	CXOM31 J004245.9+411736	GC	PB-in7	0.3
r1-2	CXOM31 J004247.0+411628	PN	Ford13	1.8
r2-56	CXOM31 J004250.3+411556	PN	Ford462	0.5
r3-71	CXOM31 J004250.6+411033	GC	mita222,PB-in2	1.2,1.8
r3-69	CXOM31 J004253.5+412553	SNR	DO80(13)	5.5
r2-9	CXOM31 J004255.5+411835	GC	Bo138	2.0
r2-6	CXOM31 J004259.5+411919	GC	Bo143	2.4
r2-5	CXOM31 J004259.8+411606	GC	Bo144	3.0
r3-96	CXOM31 J004301.6+411052	Star	SK98(237)	0.6
r2-46	CXOM31 J004301.7+411726	Star	Ha94(261262)	0.6
r2-4	CXOM31 J004302.8+411522	GC	Bo146	1.5
r3-21	CXOM31 J004302.9+412042	PN	Ford201	1.8
r3-19	CXOM31 J004303.2+412122	GC	mita240	1.3
r3-83	CXOM31 J004306.6+412243	EO	MLA93(686)	0.9
r3-18	CXOM31 J004307.4+412020	GC	mita246	1.0
r3-15	CXOM31 J004310.5+411451	GC	Bo153,mita251	2.0,1.1

Table 4—Continued

My ref.	*Chandra* Name	Type	Identification	Offset (″)
r3-112	CXOM31 J004314.2+410725	GC	Bo158	2.9
r3-105	CXOM31 J004314.5+412513	GC	Bo159,mita258	2.3,1.8
r3-10	CXOM31 J004315.4+411125	GC	mita260	0.2
r3-7	CXOM31 J004321.0+411751	PN	Ford209	1.0
r3-63	CXOM31 J004327.7+411829	SNR	MA95(2-032),DO80(15)	6.0,4.0
r3-1	CXOM31 J004337.1+411443	GC	mita299	1.4

Table 5. Cross-correlation of *Chandra* and *ROSAT* sources

My ref.	*Chandra* Name	*ROSAT* HRI Identification	Offset (″)
r3-61	CXOM31 J004207.6+411815	PF93(4)	0.7
r3-59	CXOM31 J004209.3+411745	PF93(5)	2.6
r3-58	CXOM31 J004210.1+411509	PF93(6)	2.4
r3-56	CXOM31 J004211.6+411048	PF93(7)	1.9
r3-54	CXOM31 J004212.0+411758	PF93(8)	2.9
r3-52	CXOM31 J004213.0+411836	PF93(9)	2.4
r3-50	CXOM31 J004215.0+411234	PF93(10)	3.5
r3-48	CXOM31 J004215.3+412032	PF93(11)	1.7
r3-47	CXOM31 J004215.5+411721	PF93(12)	2.4
r3-45	CXOM31 J004218.2+411223	PF93(14)	1.8
r3-44	CXOM31 J004218.5+411401	PF93(15)	2.5
r3-42	CXOM31 J004221.3+411601	PF93(17)	2.2
r3-40	CXOM31 J004222.3+411333	PF93(18)	2.3
r3-39	CXOM31 J004222.8+411535	PF93(20)	2.0
r3-38	CXOM31 J004223.0+411407	PF93(21)	2.2
r2-45	CXOM31 J004225.0+411340	PF93(22)	2.0
r2-36	CXOM31 J004225.9+411915	PF93(23)	2.5
r3-87	CXOM31 J004226.0+412552	PF93(24)	1.9
r2-35	CXOM31 J004228.1+411222	PF93(25)	3.1
r3-111	CXOM31 J004228.7+410434	PF93(26)	2.8
r2-34	CXOM31 J004231.0+411621	PF93(27)	1.4
r2-33	CXOM31 J004231.1+411939	PF93(28)	1.7
r2-32	CXOM31 J004231.9+411314	PF93(29)	2.3
r2-30	CXOM31 J004233.8+411619	PF93(32)	5.8
r2-27	CXOM31 J004235.1+412006	PF93(34)	1.9
r2-26	CXOM31 J004238.5+411603	PF93(35)	1.8
r2-25	CXOM31 J004239.4+411428	PF93(36)	2.3
r1-15	CXOM31 J004239.9+411547	PF93(37)	1.4
r2-22	CXOM31 J004240.5+411327	PF93(38)	1.8
r2-21	CXOM31 J004242.2+411445	PF93(39)	0.4
r1-14	CXOM31 J004242.3+411553	PF93(41)	1.4
r1-30	CXOM31 J004242.4+411659	PF93(40)	1.2

Table 5—Continued

My ref.	*Chandra* Name	*ROSAT* HRI Identification	Offset ($''$)
r1-13	CXOM31 J004242.9+411543	PF93(42)	2.0
r1-12	CXOM31 J004243.6+411632	PF93(43)	1.2
r1-11	CXOM31 J004243.8+411629		3.2
r1-29	CXOM31 J004243.7+411629		3.7
r1-10	CXOM31 J004244.2+411608	PF93(44)	1.8
r1-9	CXOM31 J004244.2+411607		2.4
r1-21	CXOM31 J004244.2+411605		4.2
r1-22	CXOM31 J004244.2+411614		5.5
r1-8	CXOM31 J004244.5+411618	PF93(47)	2.1
r1-4	CXOM31 J004245.0+411621		4.5
r3-29	CXOM31 J004244.7+411137	PF93(45)	2.2
r2-17	CXOM31 J004245.0+411407	PF93(46)	2.6
r1-18	CXOM31 J004246.0+411543	PF93(48)	4.6
r1-3	CXOM31 J004246.8+411615	PF93(49)	2.7
r1-2	CXOM31 J004247.0+411628	PF93(50)	1.8
r1-6	CXOM31 J004247.8+411533	PF93(52)	2.5
r3-25	CXOM31 J004248.4+412523	PF93(53)	2.0
r1-1	CXOM31 J004248.4+411521	PF93(54)	2.4
r2-14	CXOM31 J004249.1+411816	PF93(55)	1.5
r2-12	CXOM31 J004252.4+411540	PF93(58)	1.6
r2-13	CXOM31 J004252.4+411854	PF93(57)	0.5
r3-69	CXOM31 J004253.5+412553	PF93(59)	2.7
r2-11	CXOM31 J004254.8+411603	PF93(60)	2.0
r3-23	CXOM31 J004255.3+412556	PF93(61)	1.1
r2-9	CXOM31 J004255.5+411835	PF93(62)	2.0
r2-10	CXOM31 J004255.1+411836		5.0
r3-22	CXOM31 J004257.8+411104	PF93(64)	3.3
r2-7	CXOM31 J004258.2+411529	PF93(65)	2.1
r2-6	CXOM31 J004259.5+411919	PF93(66)	2.4
r2-5	CXOM31 J004259.8+411606	PF93(67)	3.0
r2-37	CXOM31 J004301.0+411351	PF93(68)	3.3
r2-4	CXOM31 J004302.8+411522	PF93(70)	2.3

Table 5—Continued

My ref.	*Chandra* Name	*ROSAT* HRI Identification	Offset ($''$)
r2-3	CXOM31 J004303.1+411528		3.9
r3-20	CXOM31 J004303.0+411015	PF93(71)	2.4
r3-19	CXOM31 J004303.2+412122	PF93(72)	3.4
r2-2	CXOM31 J004303.8+411805	PF93(73)	3.3
r3-17	CXOM31 J004308.6+411248	PF93(74)	4.5
r3-16	CXOM31 J004309.7+411901	PF93(75)	1.6
r3-15	CXOM31 J004310.5+411451	PF93(76)	1.4
r3-112	CXOM31 J004314.2+410725	PF93(77)	3.0
r3-10	CXOM31 J004315.4+411125	PF93(78)	4.2
r3-7	CXOM31 J004321.0+411751	PF93(79)	2.4
r3-63	CXOM31 J004327.7+411829	PF93(80)	2.4
r3-103	CXOM31 J004329.0+410749	PF93(81)	2.8
r3-2	CXOM31 J004334.3+411323	PF93(82)	5.6

Table 6. Average Hardness Ratios

Region	HR1	HR2
Inner bulge	0.27 ± 0.03	-0.03 ± 0.03
Outer bulge	0.30 ± 0.05	0.09 ± 0.04
Disk	0.45 ± 0.03	0.27 ± 0.04

Table 7. Variable sources in M31

Region	Detected sources	Number of variables	Fraction	Number of spectral variables	Fraction	Number of transients	Fraction
Inner bulge	33	24	73%	3	9%	5	15%
Outer bulge	59	34	58%	7	12%	5	8.5%
Disk	106	41	39%	2	2%	3	2.8%

Note. — 6 sources are excluded in the disk region as they were in the field in only one observation; the actual total detected sources in this region is 112.

Table 8. Spectral fits to the 20 brightest sources

	Power-law				Raymond-Smith [a]			
Source Number	N_H (10^{21} cm^{-2})	α	χ^2_ν/dof	Flux [b]	N_H (10^{21} cm^{-2})	kT_{RS} (keV)	χ^2_ν/dof	Flux [b]
r1-1	$2.3^{+0.7}_{-0.6}$	1.7 ± 0.2	0.8/36	1.38	1.9 ± 0.5	$7.4^{+3.3}_{-1.9}$	0.8/36	1.32
r1-5	$2.3^{+0.7}_{-0.6}$	1.6 ± 0.2	0.9/31	1.25	1.9 ± 0.6	$10.9^{+14.7}_{-4.2}$	0.9/31	1.22
r2-3	$2.7^{+0.6}_{-0.9}$	$2.5^{+0.4}_{-0.3}$	1.2/31	0.49	1.0 ± 0.5	$3.3^{+1.1}_{-0.8}$	1.5/13	0.37
r2-5	$0.5^{+0.8}_{-\infty}$	$1.1^{+0.2}_{-0.3}$	0.9/11	0.58	$0.8^{+0.7}_{-0.5}$	$64.0^{+\infty}_{-46.5}$	1.0/11	0.52
r2-6	$1.8^{+1.0}_{-0.8}$	$1.9^{+0.4}_{-0.3}$	0.7/12	0.45	0.8 ± 0.6	$7.3^{+10.5}_{-2.7}$	0.9/12	0.44
r2-11	$1.8^{+0.7}_{-0.6}$	1.8 ± 0.2	1.4/30	0.96	1.0 ± 0.5	$7.5^{+3.8}_{-1.9}$	1.5/30	0.94
r2-13	$1.8^{+0.8}_{-0.6}$	1.5 ± 0.2	1.0/33	1.31	1.6 ± 0.6	$14.8^{+28.3}_{-6.2}$	1.0/33	1.29
r2-26	$1.9^{+0.7}_{-0.5}$	1.0 ± 0.1	1.0/62	3.42	3.2 ± 0.5	$64.0^{+\infty}_{-20.3}$	1.3/62	3.07
r2-26[d]	$3.2^{+1.7}_{-1.4}$	$1.6^{+0.3}_{-0.2}$	0.8/22	3.07	$2.6^{+1.4}_{-1.1}$	$9.0^{+13.0}_{-3.5}$	0.8/22	3.00
r2-32	< 0.5	$1.3^{+0.2}_{-0.1}$	0.6/12	0.49	0.0 [c]	$48.6^{+\infty}_{-51.9}$	0.7/12	0.48
r2-34	$1.5^{+1.0}_{-0.8}$	1.9 ± 0.3	1.5/13	0.60	0.7 ± 0.6	$6.0^{+4.7}_{-1.8}$	1.5/13	0.57
r2-35	$0.9^{+0.7}_{-0.6}$	1.4 ± 0.2	1.0/22	0.89	0.7 ± 0.5	$24.4^{+\infty}_{-16.5}$	1.0/22	0.88
r3-15	0.9 ± 0.5	1.4 ± 0.2	0.9/40	1.62	$0.8^{+0.4}_{-0.2}$	$30.4^{+\infty}_{-18.3}$	0.9/40	1.60
r3-16	$2.5^{+0.2}_{-0.1}$	$1.9^{+0.5}_{-0.3}$	1.0/12	0.50	$1.4^{+0.8}_{-0.6}$	$6.2^{+5.8}_{-1.9}$	1.1/12	0.46
r3-22	2.6 ± 0.1	2.0 ± 0.3	0.7/13	0.51	$1.4^{+0.8}_{-0.6}$	$4.6^{+2.5}_{-1.3}$	0.7/13	0.45
r3-39	2.6 ± 0.1	1.8 ± 0.3	0.7/18	0.80	1.8 ± 0.7	$7.1^{+6.4}_{-2.3}$	0.8/18	0.76
r3-42	5.9 ± 0.2	$2.5^{+0.5}_{-0.4}$	0.5/11	0.65	$3.5^{+1.2}_{-0.9}$	$3.4^{+1.5}_{-0.9}$	0.6/11	0.46
r3-44	1.6 ± 0.8	1.5 ± 0.2	1.2/23	0.90	1.2 ± 0.6	$13.2^{+43.2}_{-5.9}$	1.1/23	0.87
r3-45	3.5 ± 1.0	2.8 ± 0.4	1.0/19	0.79	0.9 ± 0.5	$3.1^{+0.9}_{-0.6}$	1.6/19	0.51
r3-52	$8.5^{+0.2}_{-0.1}$	3.0 ± 0.3	0.8/26	2.05	$5.4^{+1.3}_{-0.9}$	$2.4^{+0.5}_{-0.4}$	1.1/26	1.05
r3-61	4.7 ± 0.2	1.8 ± 0.3	1.0/13	0.70	3.8 ± 1.0	$6.9^{+7.8}_{-2.3}$	0.9/13	0.67

Note. — All quoted uncertainties are 90% confidence.

[a] Fixed at solar abundence

[b] Unabsorbed flux in 0.5–10 keV (10^{-12} erg cm^{-2} s^{-1})

[c] N_H hit the minimum value of 0 allowed by XSPEC

[d] Pile-up corrected

Table 9. Luminosity functions of M31

Region	Cumulative [a]			Differential [b]	
	α_1 [c]	α_2 [d]	Break ($\times 10^{37}$ erg s^{-1})	α_1 [c]	α_2 [d]
Inner bulge	0.14 ± 0.03	0.70 ± 0.08	0.15 ± 0.04	$0.88^{+0.45}_{-0.34}$	0.73 ± 0.25
Outer bulge	0.22 ± 0.03	0.93 ± 0.13	$0.57^{+0.18}_{-0.12}$	$0.55^{+0.17}_{-0.15}$	$1.00^{+0.45}_{-0.34}$
Bulge	0.29 ± 0.02	1.12 ± 0.15	$0.89^{+0.21}_{-0.17}$	0.50 ± 0.10	$1.15^{+0.43}_{-0.33}$
Disk	0.43 ± 0.02	$2.0^{+0.46}_{-0.40}$	$1.77^{+0.37}_{-0.27}$	$0.51^{+0.15}_{-0.12}$	$2.17^{+0.91}_{-0.72}$
Integrated	0.38 ± 0.01	1.63 ± 0.20	1.69 ± 0.24	$0.47^{+0.07}_{-0.05}$	$1.63^{+0.56}_{-0.45}$

[a] $N(>L) = K_1 L^{-\alpha}$ where K_1 is normalization

[b] $\frac{dN}{dL} = K_2 L^{-(\alpha+1)}$ where K_2 is normalization

[c] Power-law slope below the break

[d] Power-law slope above the break

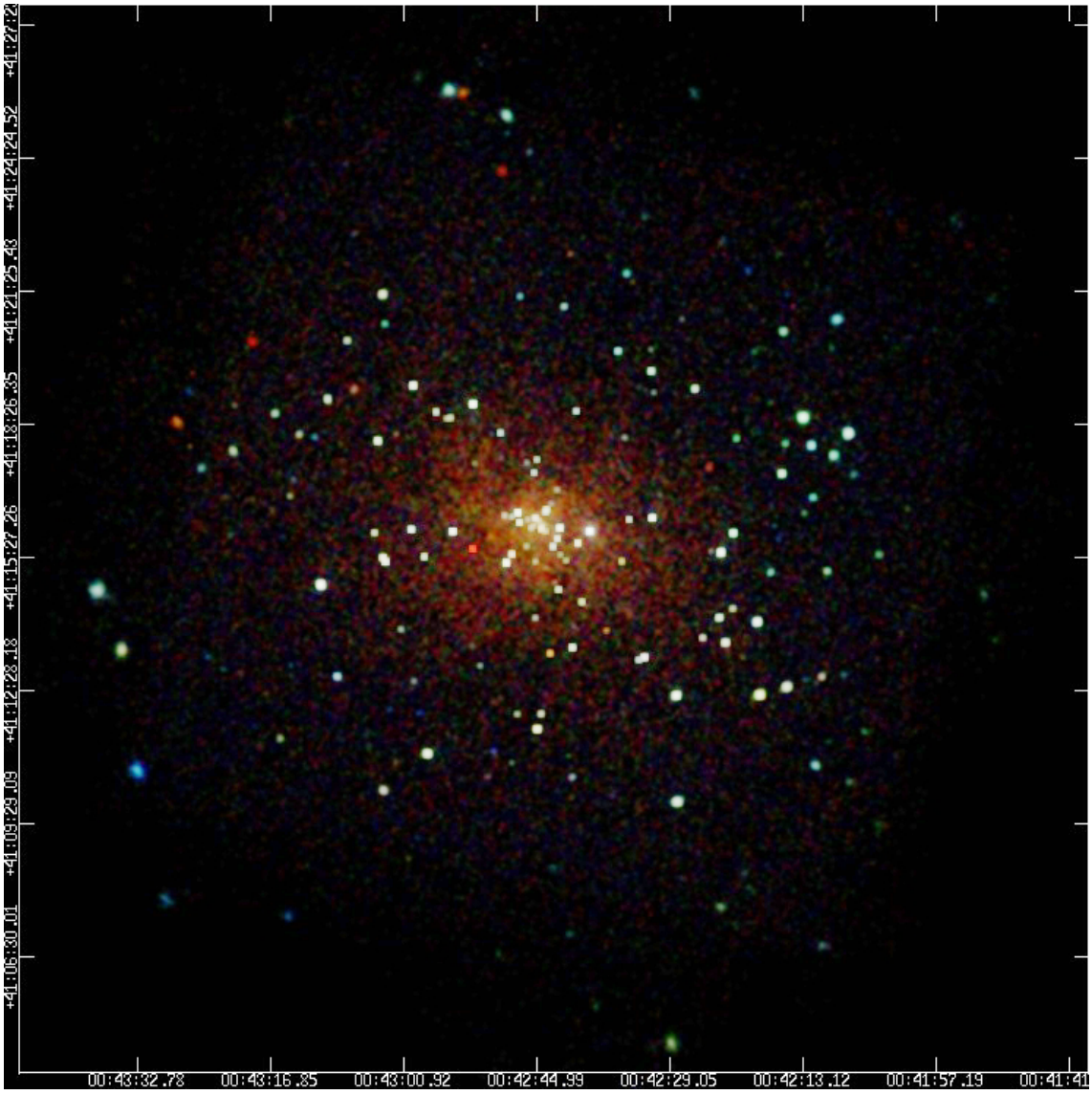

Fig. 1.— Stacked "true color" *Chandra* ACIS-I image (39.7 ks) of the central $\sim 17' \times 17'$ region of M31. This image was constructed from the soft (red; 0.3–1 keV), medium (green; 1–2 keV) and hard (blue; 2–7 keV) energy bands. The pixel size is $1.96''$ and the image has been smoothed with a 1σ Gaissian function.

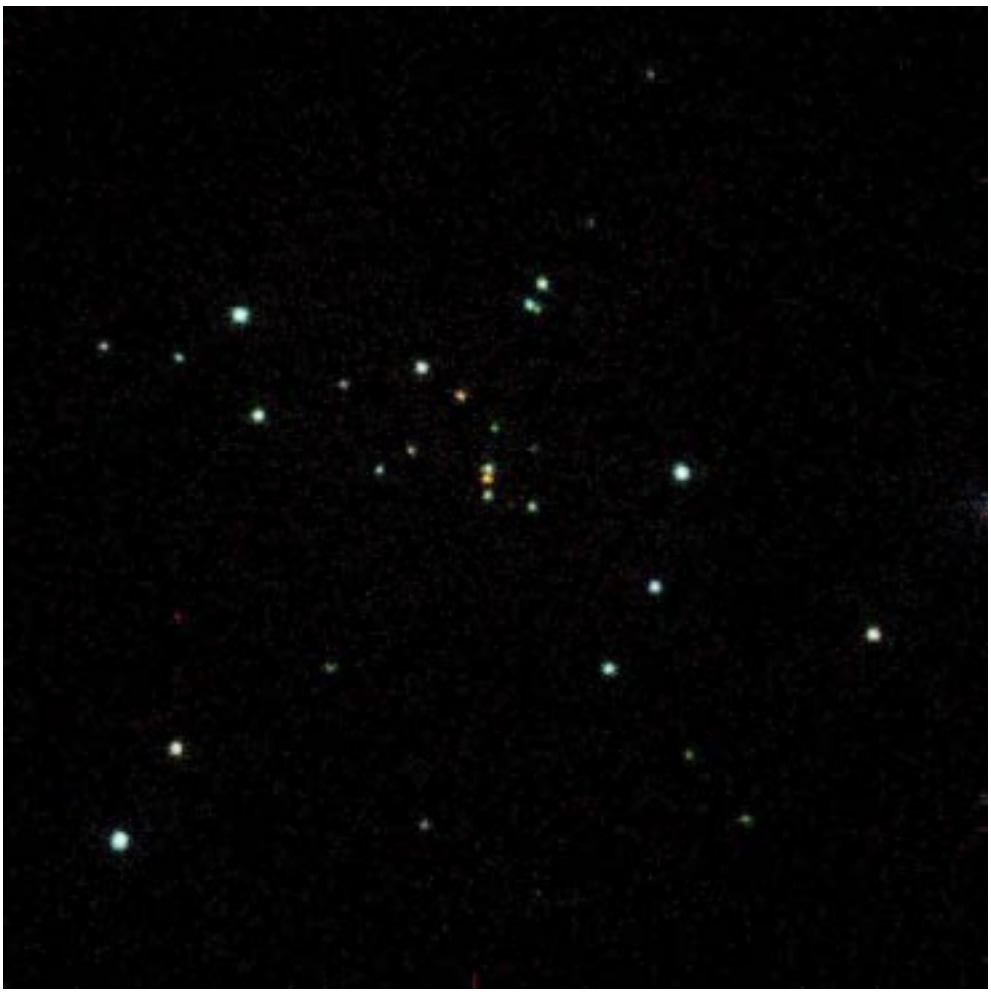

Fig. 2.— Stacked "true color" *Chandra* ACIS-I image of the central $\sim 2' \times 2'$ region ("region 1") of M31. The color representation is the same as Figure 1 and the pixel size is $0.123''$. M31* candidate is marked.

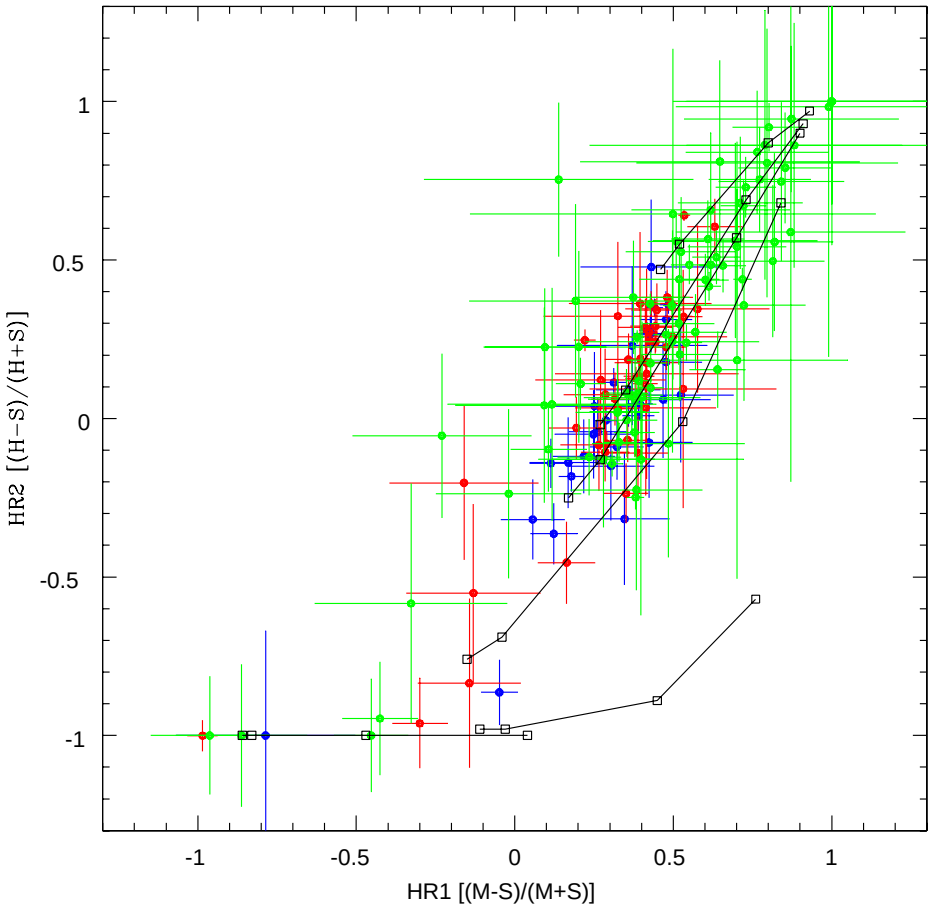

Fig. 3.— Color-color diagram for all sources with more than 20 counts. Color symbols represent different regions of the field: region 1 (blue); region 2 (red) and region 3. Also plotted are the estimated hardness ratios estimated from different spectral models. From top to bottom: power-law model with α of 1, 1.7, 2 and 3, and blackbody model with kT of 0.2 keV and 0.1 keV. For each model, N_H varies from the left from 5×10^{20}, 10^{21}, 5×10^{21} and 10^{22}.

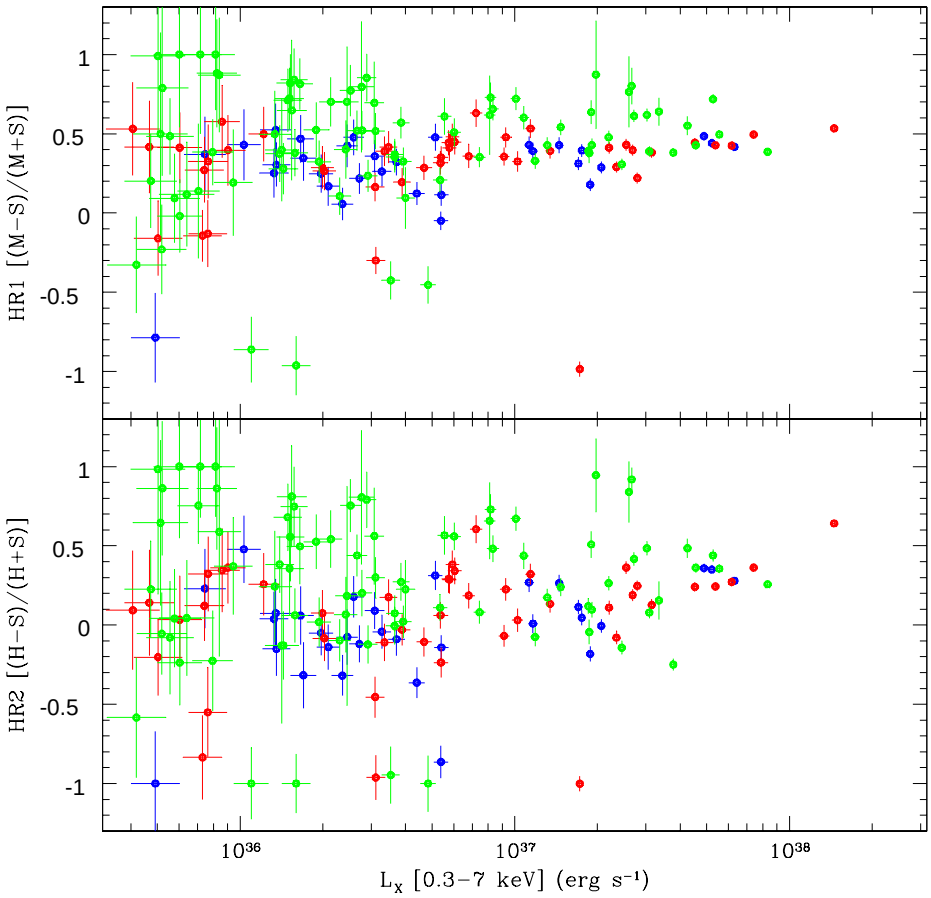

Fig. 4.— Hardness-intensity diagram for all sources with more than 20 counts. Color symbols are the same as Fig. 3.

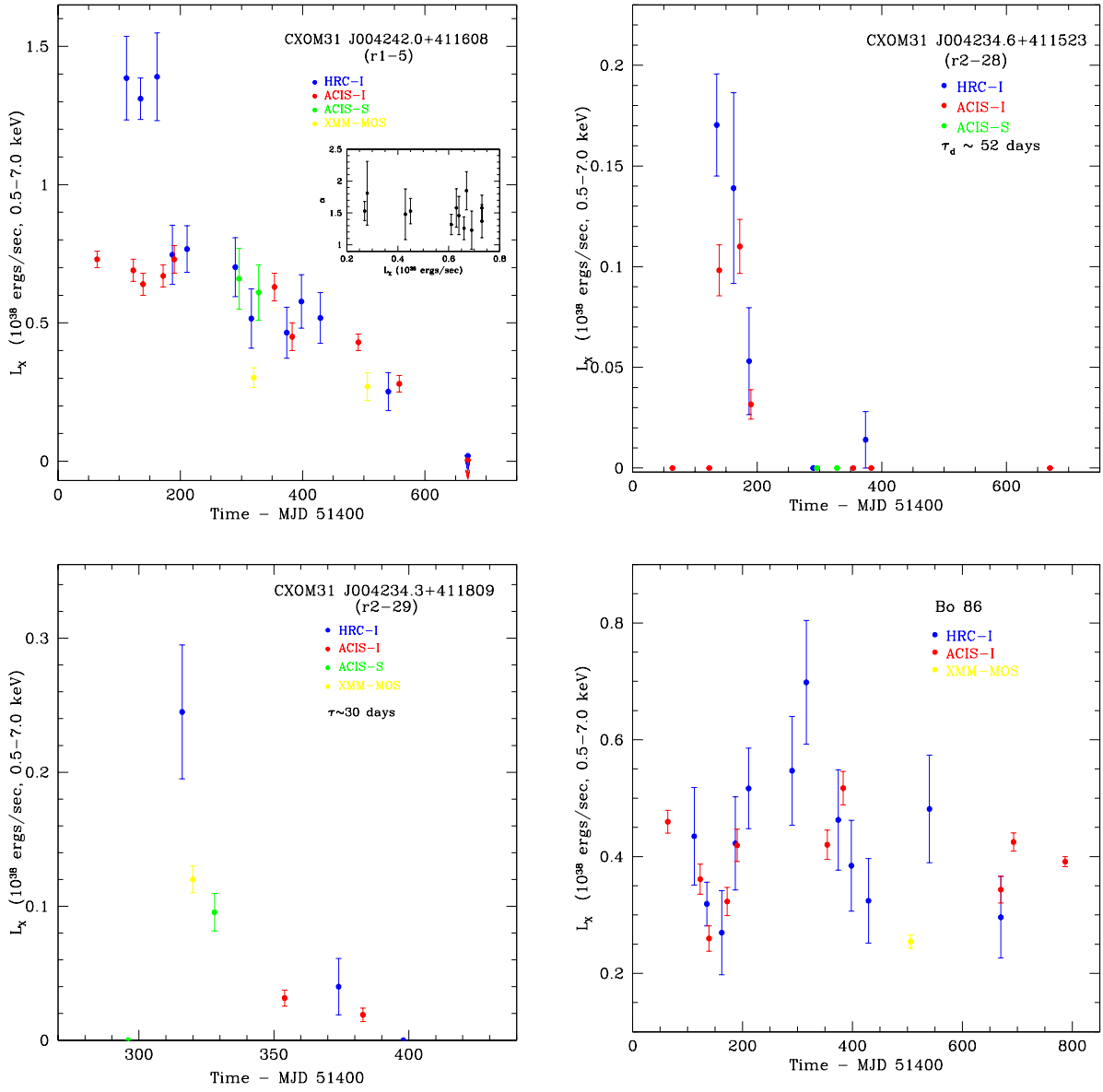

Fig. 5.— Light curves of 3 bright transients and globular cluster Bo 86 as seen in the past two years with *Chandra*. Observations from HRC-I, ACIS-S and XMM-MOS are included. The inset of r1-5 shows that the energy spectrum during the whole outburst is consistent with a power-law with slope of ~ 1.5 (see also Trudolyubov, Borozdin, & Priedhorsky 2001). It is worth noting that the three HRC-I data points during the early stage of the outburst indicate that the source underwent flarings or state transitions.

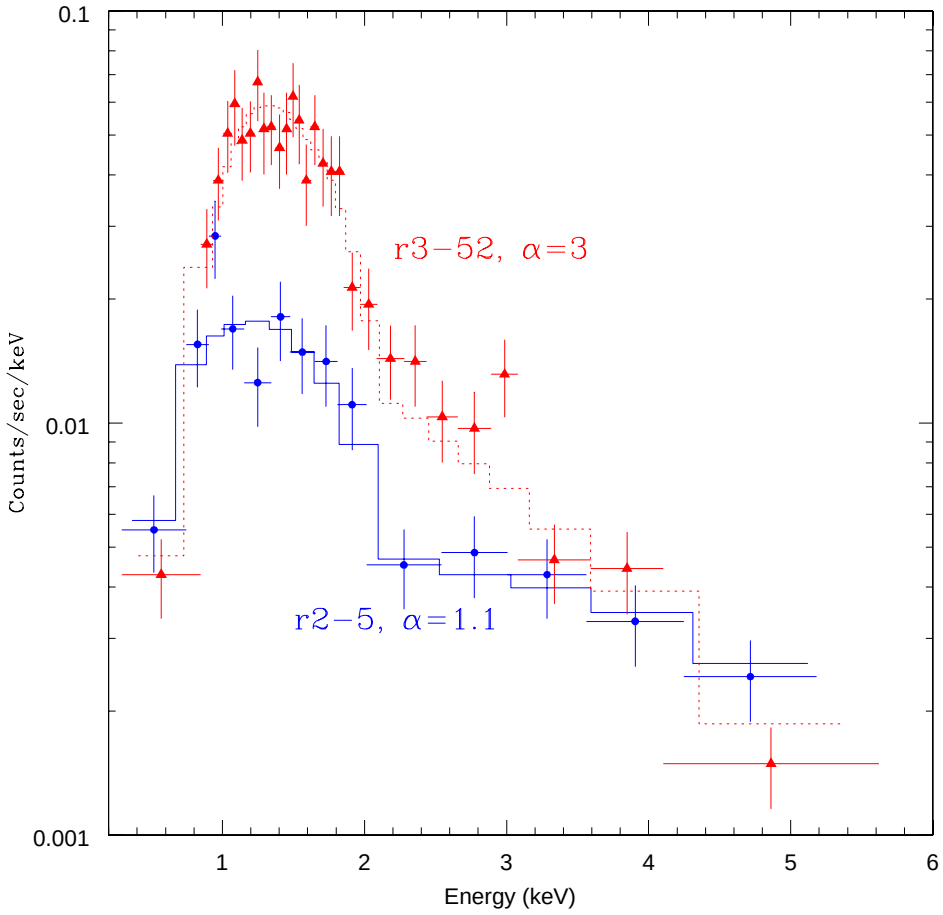

Fig. 6.— The softest (r3-52; triangles) and the hardest (r2-5; circles) energy spectra from the 20 brightest X-ray sources in the first observation.

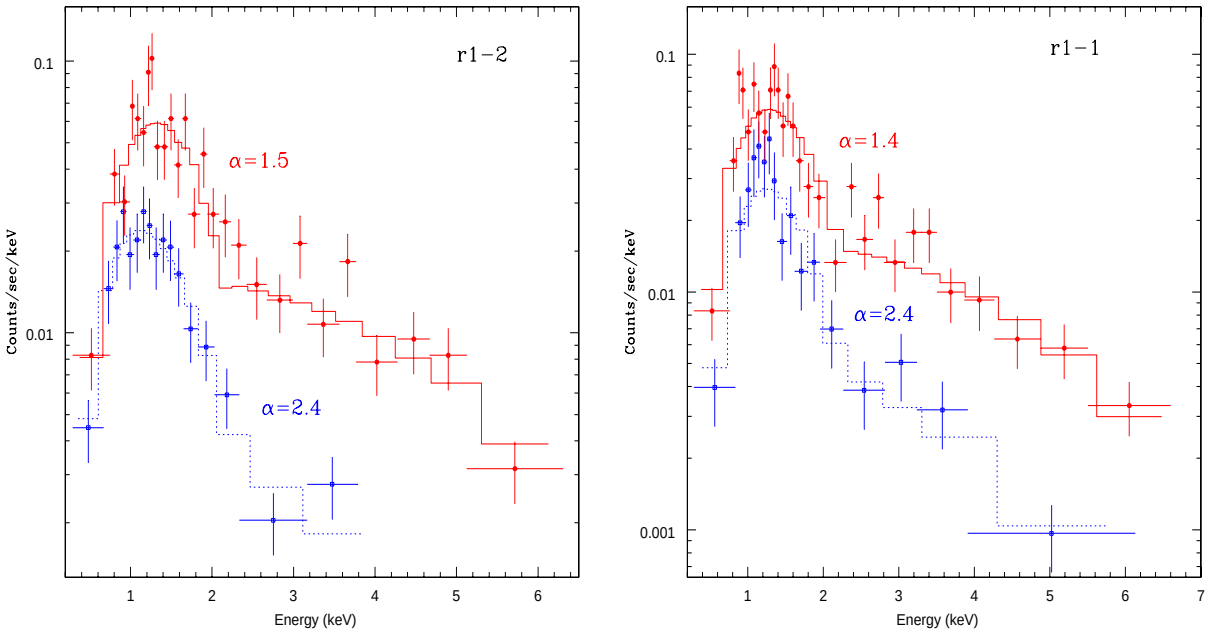

Fig. 7.— Spectral changes of two of the sources. They change from lower luminosity at softer state to higher luminosity with harder state.

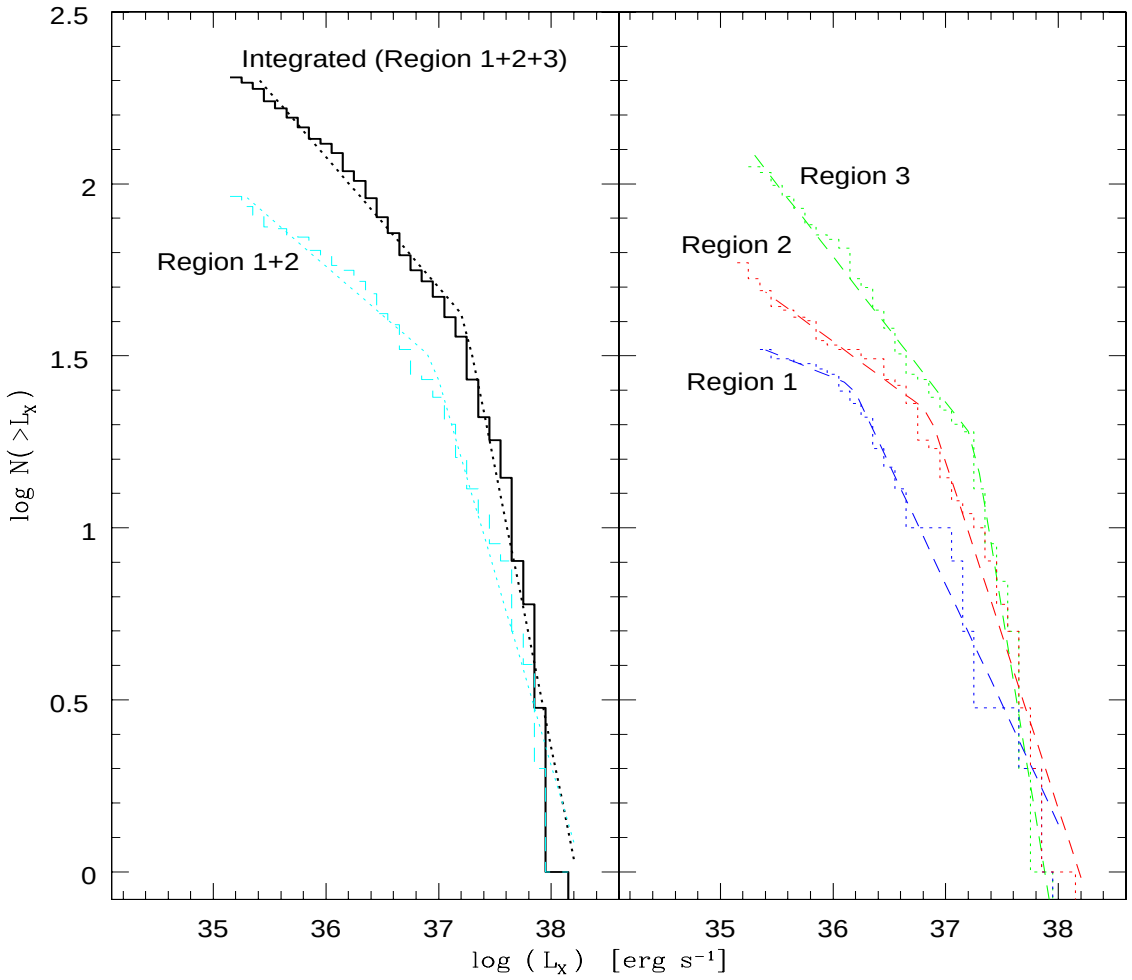

Fig. 8.— Left: Luminosity functions for all sources (Regions 1+2+3) and bulge (Regions 1+2). Right: Luminosity functions for inner bulge (Region 1), outer bulge (Region 2) and disk (Region 3).